Bulletin of the JSME Vol.10, No.2, 2023
Mechanical Engineering Journal

Maximization of the fundamental eigenfrequency using topology optimization based on multi-material level set method

Nari NAKAYAMA*, Hao LI*, Kozo FURUTA*, Kazuhiro IZUI* and Shinji NISHIWAKI*
* Department of Mechanical Engineering and Science, Kyoto University
Kyotodaigaku-katsura CIII, Nishikyo-ku, Kyoto 615-8540, Japan
E-mail: nakayama.nari.42z@st.kyoto-u.ac.jp

Received: 26 August 2022; Revised: 13 December 2022; Accepted: 20 February 2023

Abstract
A multi-material structure that is composed of several different material properties is promising for achieving an ideal functionality that can outperform a single material structure. In the course of automotive design, the combination of lightweight and stiff materials can reduce the weight of a car body without sacrificing its performance. This paper proposes a multi-material topology optimization (MMTO) framework for the eigenfrequency maximization problem based on the Multi-material level set (MMLS) based topology optimization. The key idea of MMLS is to use M level set functions to represent M material regions and one void region without overlap. To demonstrate the proposed method, first, we formulate an MMTO problem for maximizing the eigenfrequency based on the shape representation by the MMLS method. Next, we derive the topological derivatives of multiple materials in the eigenfrequency problem and construct an optimization algorithm in which the level set functions are evolved by solving a reaction–diffusion equation (RDE) based on the topological derivatives. Several numerical examples are provided to validate the proposed methodology.

Keywords : Eigenfrequency, Multi-material structure, Topology optimization, Multi material level–set method, Topological derivative

1. Introduction

Multi-material structure composed of several different material properties has been widely used to improve structural functionalities due to its being an innovative structural configuration. The multi-material design has attracted great interest from academia and industry. The key idea behind this is to place the “right” material in its ”right” place in order to achieve an ideal functionality that can outperform a single material design. For example, in the course of automotive design, the combination of lightweight and stiff materials can reduce the weight of a car body without sacrificing its performance (Goede et al., 2009). There are also reports of metamaterials with negative thermal expansion coefficients produced by designing microstructures with multiple materials (Sigmund and Torquato, 1997). In addition, the rapid development of additive manufacturing technology makes it possible to use multiple materials at the same time to fabricate one single objective.

As is well-known, unlike the traditional size or shape optimization methods, topology optimization (TO) has a higher design flexibility, which can attain any shape or topological configuration within a given design space. During the past few decades, TO techniques have undergone a tremendous development in various directions and multiphysics fields, such as thermal device design (Yamada et al, 2011), thermal-fluidic device design (Li et al, 2022a), electromagnetic metamaterial design (Otomori et al., 2012), acoustic metamaterial design (Noguchi et al., 2018), etc. The TO methods can be broadly classified into the homogenization design method (Bendsøe and Kikuchi, 1988), density method (Bendsøe and Sigmund, 1999), evolutionary structural optimization (ESO) approach (Xie and Steven, 1993), level set-based method (Wang et al., 2003; Allaire et al., 2004; Yamada et al., 2010), and other feature driven methods such as the moving morphology component (MMC) method (Guo et al., 2014a) and the moving wide Bezier components with constrained ends (MWBCE) method (Zhu et al., 2021).

Paper No.22-00353
J-STAGE Advance Publication date : 2 March, 2023
[DOI: 10.1299/mej.22-00353]

Among these methods, the level set-based methods (LSM) are capable of expressing the boundaries of the structure as the iso-surface of a level set function. Therefore, it has the advantage of obtaining clear boundaries in between different material phases. The LSM has been developed in several different directions. The common method is to update the level set function by solving the Hamilton-Jacobi equation (Want et al., 2003; Allaire et al., 2004). In this method, the zero iso-surfaces of the level set function are moved based on the shape derivative. Different from that, Yamada et al. (2010) proposed a reaction-diffusion equation-based (RDE) level set method. In this method, the level set function is varied based on topological derivatives, which allow for not only shape but also topological changes such that new holes can be created during the optimization process. In the recent work by Li et al. (2022b), they demonstrated the RDE method by solving a fluid–structure interaction problem where the moving boundary between the fluid and solid phases can be explicitly captured by the body-fitted adaptive mesh while the holes can be created inside the design domain.

Combining the idea of the LSM with multi-material design, Wang and Wang (2004) proposed a "color" level set method, which represents 2^M material regions with M level set functions. They applied this method to solve the mean compliance minimization problem, and this method was later applied to other TO problems such as compliant mechanism design (Wang et al, 2005) and stress-related optimization problems (Guo et al., 2014b). In their later works, Wang and Wang (2009) proposed a piecewise constant level set method. This method can describe multiple material phases with only one piecewise constant level-set function. Luo et al. (2009) applied this method to the design of piezoelectric actuators. Unlike the aforementioned "color" level set method, in the Multi-Material Level Set (MMLS) method proposed by Wang et al. (2015), they represented $(M + 1)$ material phases with M level set functions, and they used a Hamilton-Jacobi equation to vary the level set functions. Using the same level set boundary expression, Cui et al. (2016) and Kishimoto et al. (2017) adopted a reaction–diffusion equation for updating the level set functions.

Although the MMLS method has grown mature in the field of structural optimization problems, to date, there is still a lack of research reporting on the MMTO for the eigenfrequency problems. Indeed, most of the existing works present only single-material designs using different TO methods, e.g., the homogenization based approach (Díaaz and Kikuchi, 1992), ESO method (Xie and Steven, 1996), density-based approach (Pedersen, 2000), and LSM (Allaire et al., 2005; Yamada et al., 2010).

Aiming at the research gaps as mentioned above, this work presents a new framework for MMTO based on the MMLS method for the eigenfrequency maximization problem. First, we formulate MMTO in two ways: (1) MMTO with concentrated masses and (2) MMTO under mean compliance constraint. Next, we use the MMLS method to represent multiple material phases without overlap, and the boundaries between each material can be clearly described. Then, the level set functions are updated using a reaction-diffusion equation with the topological derivative as the reaction term, which allows for the creation of new holes during optimization. We derive the topological derivatives and numerically validate the correctness of the deduced results. Several two-dimensional numerical examples are presented to confirm the validity of the proposed methodology.

The rest of this paper is arranged as follows. In Section 2, we formulate the MMTO problem based on the shape representation using the MMLS method for eigenfrequency maximization. In Section 3, we perform sensitivity analysis based on topological derivatives. In Section 4, we construct a TO algorithm using the finite element method. In Section 5, the validity of the proposed methodology is verified by numerical examples. Finally, conclusions are given in Section 6.

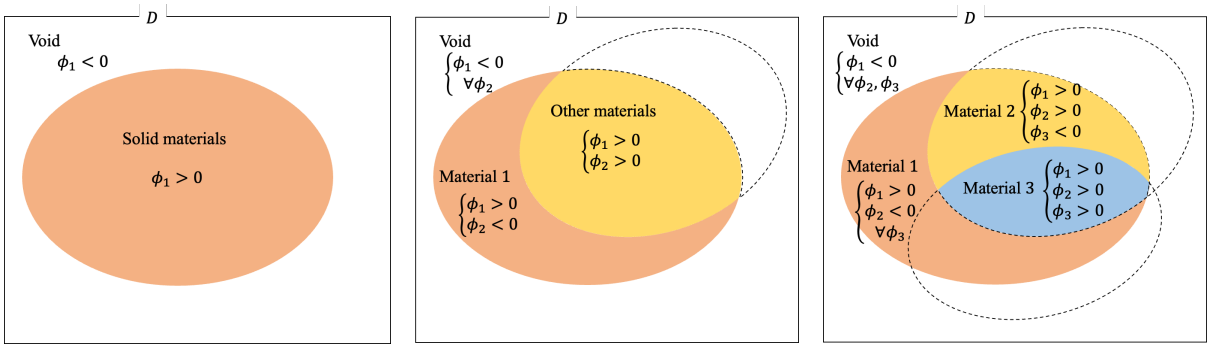

(a) ϕ_1. (b) ϕ_1 and ϕ_2. (c) ϕ_1, ϕ_2, and ϕ_3.

Fig. 1 Schematic diagram of the MMLS method for the case of three-phase material.

[DOI: 10.1299/mej.22-00353]

2. Formulation

2.1. Governing equations of eigenfrequency problem

We consider a computational domain $\Omega \subset \mathbb{R}^2$ which consists of several subdomains $\Omega_i\,(i = 1, \ldots, M)$ where each subdomain is composed of material phase i. With the assumption of the isotropic linear elastic material, the governing equations underlying the mth eigenvalue $\lambda_{(m)}$ and the corresponding eigenmode $U_{(m)i}$ can be formulated as the following boundary value problem:

$$C^{(i)}_{ijkl}\frac{\partial^2 U_{(m)k}}{\partial x_l \partial x_j} + \lambda_{(m)}\rho^{(i)}U_{(m)i} = 0 \text{ in } \Omega_i \tag{1a}$$

$$U^{(i)}_{(m)i} - U^{(j)}_{(m)i} = 0 \text{ on } \Gamma_{i,j} \tag{1b}$$

$$C^{(i)}_{ijkl}\frac{\partial U^{(i)}_{(m)k}}{\partial x_l}n^{(i)}_j + C^{(j)}_{ijkl}\frac{\partial U^{(j)}_{(m)k}}{\partial x_l}n^{(j)}_j = 0 \text{ on } \Gamma_{i,j} \tag{1c}$$

$$U_{(m)i} = 0 \text{ on } \Gamma_u \tag{1d}$$

$$C_{ijkl}\frac{\partial U_{(m)k}}{\partial x_l}n_j = 0 \text{ on } \Gamma_n, \tag{1e}$$

where the eigenvalue is equal to the square of the eigenfrequency $\lambda_{(m)} = \omega^2_{(m)}$. Γ_u is the Dirichlet boundary where the structure is fixed, Γ_n is the Neumann boundary, and $\Gamma_{i,j}$ denotes the interface between Ω_i and Ω_j.

The superscript (i) represents the quantities in the domain Ω_i and $\boldsymbol{n}^{(i)}$ represents the unit normal vector on $\Gamma_{i,j}$ oriented from Ω_i to Ω_j. Eqs. (1b) and (1c) represent continuity of the eigenmode and stress, respectively. $C^{(i)}_{ijkl}$ and $\rho^{(i)}$ represent the elastic tensor and mass density, respectively. The elastic tensor of isotropic linear elastic materials in two-dimensional plane stress problems is given by

$$C^{(i)}_{ijkl} = \frac{\nu^{(i)}E^{(i)}}{1-\nu^{(i)2}}\delta_{ij}\delta_{kl} + \frac{E^{(i)}}{2(1+\nu^{(i)})}(\delta_{ik}\delta_{jl} + \delta_{jk}\delta_{il}), \tag{2}$$

where $E^{(i)}$ is Young's modulus and $\nu^{(i)}$ is Poisson's ratio. The eigenmodes are normalized as

$$\sum_{i=1}^{M}\int_{\Omega_i}(\rho^{(i)}U_{(m)i}U_{(m)i})d\Omega = 1. \tag{3}$$

2.2. Multi-material level set boundary expression

Here we examine the basic concept of the the multi-material level set (MMLS) method. Let us consider a computational domain $D \subset \mathbb{R}^2$, which is composed of multiple solid phases $\Omega_i \subset D\,(i = 1, \ldots, M)$, together with a void phase $\Omega_0 = D\backslash\Omega_i$. They can be represented by a set of implicit level set functions $\phi_i\,(\boldsymbol{x})\,(i = 1, \ldots, M)$, as follows:

$$\begin{cases} \phi_1(\boldsymbol{x}) < 0 & \text{if } \boldsymbol{x} \in \Omega_0 \\ \phi_2(\boldsymbol{x}) < 0,\ \phi_1(\boldsymbol{x}) > 0 & \text{if } \boldsymbol{x} \in \Omega_1 \\ \quad\vdots & \\ \phi_{i+1}(\boldsymbol{x}) < 0,\ \phi_j(\boldsymbol{x}) > 0\ (1 \le j \le i) & \text{if } \boldsymbol{x} \in \Omega_i\ (i = 1, \ldots, M-1) \\ \quad\vdots & \\ \phi_j > 0\ (1 \le j \le M) & \text{if } \boldsymbol{x} \in \Omega_M. \end{cases} \tag{4}$$

Let us take the case of $M = 3$ as an example. The schematic diagram of the multiple level set function is shown in Fig. 1. As shown in Fig. 1a, the first level set function $\phi_1(\boldsymbol{x})$ is used to identify the presence or the absence of the solid phase (regardless of which material). Next, the second level set function $\phi_2(\boldsymbol{x})$ is used to distinguish between solid phase #1 from other solid phases (solid phases #2 and #3). In the same way, solid phase #2 can be identified based on the third level set function $\phi_3(\boldsymbol{x})$.

2.3. Interpolation of material properties

We define the following characteristic functions $\psi_i(\boldsymbol{x})\ (i = 0, \ldots, M)$:

$$\psi_i(\boldsymbol{x}) = \begin{cases} 1 & \boldsymbol{x} \in \Omega_i \\ 0 & \boldsymbol{x} \notin \Omega_i. \end{cases} \tag{5}$$

[DOI: 10.1299/mej.22-00353]

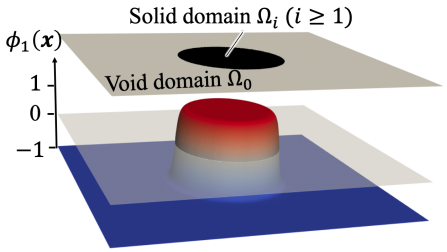

Fig. 2 Schematic of the level set function.

$\psi_i(\boldsymbol{x})$ can be expressed by the level set functions $\phi_i(\boldsymbol{x})$, as follows:

$$\begin{cases} \psi_0(\boldsymbol{x}) = 1 - H(\phi_1) \\ \psi_1(\boldsymbol{x}) = (1 - H(\phi_2))\, H(\phi_1) \\ \quad \vdots \\ \psi_i(\boldsymbol{x}) = (1 - H(\phi_{i+1}))\, \prod_{i=1}^{j} H(\phi_j) \quad (i = 1, ..., M-1) \\ \quad \vdots \\ \psi_M(\boldsymbol{x}) = \prod_{j=1}^{M} H(\phi_j), \end{cases} \tag{6}$$

where $H(\phi)$ is a heaviside function defined as

$$H(\phi) = \begin{cases} 1 & \text{if } \phi \geq 0 \\ 0 & \text{if } \phi < 0. \end{cases} \tag{7}$$

The elasticity tensor and mass density can be interpolated using the characteristic function $\psi_i(\boldsymbol{x})$, as follows:

$$\begin{cases} C_{ijkl}(\boldsymbol{x}) = \sum_{i=1}^{M} C_{ijkl}^{(i)} \psi_i(\boldsymbol{x}) \\ \rho(\boldsymbol{x}) = \sum_{i=1}^{M} \rho^{(i)} \psi_i(\boldsymbol{x}). \end{cases} \tag{8}$$

2.4. RDE-based level set method

In this paper, we use the level set-based topology optimization proposed by Yamada et al. (2010), in which a reaction diffusion equation (RDE) is used to update the level set functions based on the topological derivatives. The topological derivatives will be explained in detail in Section 3.

The level set functions used here are not the signed distance functions widely used in shape optimization problems. For the regularization terms used to regularize the optimization problem, which will be explained later, the level set functions have upper and lower limits, as follows:

$$-1 \leq \phi_i(\boldsymbol{x}) \leq 1. \tag{9}$$

To update the level set function ϕ_i based on the topological derivatives, we introduce a fictitious time t and assume that the partial derivative of the level set function ϕ_i with respect to t is proportional to $\bar{F}'^{(i)}$, the functional derivative of $\bar{F}$ with respect to ϕ_i. Then the following time evolution equation can be obtained:

$$\frac{\partial \phi_i}{\partial t} = -\bar{F}'^{(i)}, \tag{10}$$

With Eq. (10), the Lagrangian monotonically decreases with the time evolution (Li et al., 2021). In order to regularize the above optimization problem which is an ill-posed problem, a diffusive term is introduced, as follows:

$$\frac{\partial \phi_i}{\partial t} = -\left(\bar{F}'^{(i)} - \tau_i \nabla^2 \phi_i\right), \tag{11}$$

where τ_i $(i = 1, \ldots, M)$ is the regularization parameter. This is a reaction-diffusion equation, and the diffusion term guarantees the smoothness of the level set functions. The upper and lower limits are imposed on the level set functions so that the regularization effect works only near the boundaries, where the gradient of the level set functions is large,

[DOI: 10.1299/mej.22-00353]

as shown in Fig. 2. Therefore, the complexity of the optimal structure can be controlled by adjusting the value of the regularization parameters. Furthermore, we assume that the boundary condition for the level set functions is a Neumann boundary condition. Therefore, the time evolution equation and boundary conditions are expressed as

$$\begin{cases} \dfrac{\partial \phi_i}{\partial t} = -\left(\bar{F}'^{(i)} - \tau_i \nabla^2 \phi_i\right) \text{ in } D \\ \dfrac{\partial \phi_i}{\partial x_j} n_j = 0 \text{ on } \partial D. \end{cases} \tag{12}$$

2.5. Optimum design problem

The simplest objective function for the maximization of the fundamental eigenfrequency can be formulated as

$$\inf_{\Omega_1,\ldots,\Omega_M} F(\Omega_1,\ldots,\Omega_M) = -\lambda_{(1)} = -\omega_{(1)}^2. \tag{13}$$

One of the major issues of eigenfrequency problems in topology optimization is that the order of the eigenvalues may change during the optimization. Therefore, in the above objective function, when the mode of the fundamental eigenvalue is swapped, the design sensitivity becomes discontinuous and may lead to an oscillation of the objective value. One of the solutions is to trace the desired mode shape during the optimization process. For example, Kim and Kim (2000) proposed a method to examine the mode assurance criterion (MAC) value between each extracted mode of the updated structure and the desired mode. In contrast to the mode-tracking method using MAC value, which requires defining the desired mode shape in the entire computational domain and comparing it to the eigenmodes, Maeda et al. (2006) proposed a method to control the mode shape by specifying the portion of the mode shape where the desired dynamic response is to be maximized or minimized. An alternative method is to define an objective function with multiple eigenvalues so that the design sensitivity does not become discontinuous even if the mode switching occurs among the selected eigenvalues in the process of optimization. Ma et al. (1995) proposed the mean-eigenvalue, which is a combination of multiple eigenvalues, as the objective function. We follow the lead of Ma et al. and define the objective function as the harmonic mean of the first n eigenvalues as follows:

$$\inf_{\Omega_1,\ldots,\Omega_M} F(\Omega_1,\ldots,\Omega_M) = -\left(\sum_{m=1}^{n} \frac{1}{\omega_{(m)}^2}\right)^{-1} = -\left(\sum_{m=1}^{n} \frac{1}{\lambda_{(m)}}\right)^{-1}. \tag{14}$$

In conventional topology optimization problems for maximizing the fundamental eigenfrequency, it is common to place concentrated masses. This is because, without concentrated masses, this design problem becomes an ill-posed problem in which the solid material is prone to move closer to the fixed walls Γ_u, and eventually only infinitesimally thin structures will remain. (Pedersen, 2000). However, since concentrated masses are not real materials, the formulation with concentrated masses is difficult to apply to real design problems. Therefore, instead of using concentrated masses, we propose to use stiffness constraints against static traction, since it is more realistic to maximize the fundamental eigenfrequency while maintaining stiffness against traction, and as shown in the numerical example, imposing stiffness constraints can prevent the design problem from being an ill-posed problem. In Section 2.5.1, the conventional eigenfrequency maximization problem is formulated with concentrated masses, and in Section 2.5.2, the design problem is formulated using the static mean compliance constraint. In both formulations, the volume constraints are taken into account.

2.5.1. Maximization of the fundamental eigenfrequency with concentrated masses

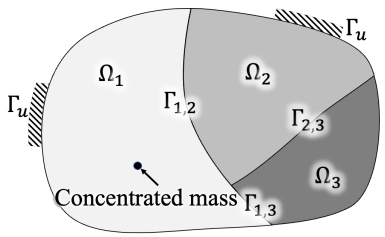

Fig. 3 Schematic of the eigenfrequency optimization problem with a concentrated mass.

The first optimum design problem is the multi-material topology optimization problem for the maximization of the

[DOI: 10.1299/mej.22-00353]

fundamental eigenfrequency with concentrated masses. The optimization problem can be formulated as

$$\begin{aligned} &\inf_{\phi_1,\ldots,\phi_M} F(\phi_1,\ldots,\phi_M) = -\left(\sum_{m=1}^{n}\frac{1}{\lambda_{(m)}}\right)^{-1} \\ &\text{s.t. } G_k(\phi_1,\ldots,\phi_M) = \frac{\int_D \psi_k \, d\Omega}{\int_D d\Omega} - V_{max}^k \le 0 \quad (k = 1,\cdots,M). \end{aligned} \tag{15}$$

where V_{max}^k is the maximum allowed volume fraction of the material k in the fixed design domain. The above optimization problem can be replaced with an unconstrained optimization problem using the Lagrangian's method of undetermined multipliers, as follows:

$$\inf_{\phi_1,\ldots,\phi_M} \bar{F}(\phi_1,\ldots,\phi_M) = F(\phi_1,\ldots,\phi_M) + \sum_{k=1}^{M}(\mu_k G_k(\phi_1,\ldots,\phi_M)) \tag{16}$$

where $\bar{F}$ is the Lagrangian and $\mu_k \ge 0$ $(k = 1,\cdots,M)$ is the Lagrange multiplier.

2.5.2. Maximization of the fundamental eigenfrequency under mean compliance constraint

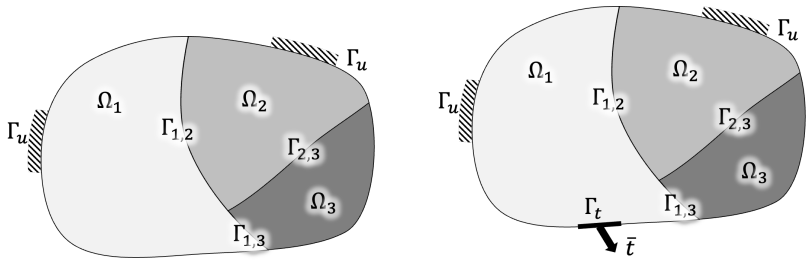

(a) Eigenfrequency problem. (b) Static problem.

Fig. 4 Schematic of the eigenfrequency optimization problem under mean compliance constraint.

In this section, in addition to the eigenfrequency problem, as shown in Fig. 4a, we consider a static problem where the surface traction is applied on the surface Γ_t, as shown in Fig. 4b. The governing equations underlying the static displacement u_i can be then formulated as the following boundary value problem:

$$C_{ijkl}^{(i)}\frac{\partial^2 u_k}{\partial x_l \partial x_j} = 0 \text{ in } \Omega_i \tag{17a}$$

$$u_i^{(i)} - u_i^{(j)} = 0 \text{ on } \Gamma_{i,j} \tag{17b}$$

$$C_{ijkl}^{(i)}\frac{\partial u_k^{(i)}}{\partial x_l}n_j^{(i)} + C_{ijkl}^{(j)}\frac{\partial u_k^{(j)}}{\partial x_l}n_j^{(j)} = 0 \text{ on } \Gamma_{i,j} \tag{17c}$$

$$u_i = 0 \text{ on } \Gamma_u \tag{17d}$$

$$C_{ijkl}\frac{\partial u_k}{\partial x_l}n_j = \bar{t}_i \text{ on } \Gamma_t, \tag{17e}$$

$$C_{ijkl}\frac{\partial u_k}{\partial x_l}n_j = 0 \text{ on } \Gamma_n, \tag{17f}$$

where Γ_u is the Dirichlet boundary where the structure is fixed, Γ_t is the Neumann boundary where traction $\bar{t}_i$ is applied, and $\Gamma_n = \Gamma/\Gamma_u \cup \Gamma_t$ is the Neumann boundary. The mean compliance is defined as $\int_{\Gamma_t} u_i \bar{t}_i \, d\Gamma$. By imposing the upper limit to the mean compliance, the optimal structure can maximize the the fundamental eigenfrequency while maintaining stiffness against traction $\bar{t}_i$. Then, the multi-material topology optimization problem for the maximization of the fundamental eigenfrequency under the mean compliance constraint can be formulated as

$$\begin{aligned} &\inf_{\phi_1,\ldots,\phi_M} F(\phi_1,\ldots,\phi_M) = -\left(\sum_{m=1}^{n}\frac{1}{\lambda_{(m)}}\right)^{-1} \\ &\text{s.t.} \begin{cases} G_k(\phi_1,\ldots,\phi_M) = \dfrac{\int_D \psi_k \, d\Omega}{\int_D d\Omega} - V_{max}^k \le 0 \quad (k = 1,\cdots,M) \\ Gc(\phi_1,\ldots,\phi_M) = \dfrac{\int_{\Gamma_t} u_i \bar{t}_i \, d\Gamma}{C_{init}} - C_{max} \le 0 \end{cases} \end{aligned} \tag{18}$$

[DOI: 10.1299/mej.22-00353]

where C_{init} is the value of mean compliance of the initial guess and C_{max} is the ratio of the maximum allowed mean compliance to C_{init}. The above optimization problem can be replaced with an unconstrained optimization problem using the Lagrangian's method of undetermined multipliers, as follows:

$$\inf_{\phi_1,\ldots,\phi_M} \bar{F}(\phi_1,\ldots,\phi_M) = F(\phi_1,\ldots,\phi_M) + \sum_{k=1}^{M} (\mu_k G_k(\phi_1,\ldots,\phi_M)) + \mu_{M+1} Gc(\phi_1,\ldots,\phi_M), \tag{19}$$

where $\bar{F}$ is the Lagrangian and $\mu_k \geq 0$ $(k = 1, \cdots, M+1)$ is the Lagrange multiplier.

3. Sensitivity analysis

3.1. Topological derivatives for eigenfrequency maximization problem

For the multi-material optimization problem formulated in Section 2, we conduct sensitivity analysis based on the concept of the topological derivatives. A topological derivative is a functional derivative of a functional with respect to an infinitesimal change in its topology. In the context of multi-material topology optimization, it indicates that the material phase in Ω_ϵ is replaced by another phase. Assuming that Ω_ϵ is a circular domain with an infinitesimal radius ϵ centered at $\boldsymbol{z} \in \Omega_a$ and the material which fills Ω_ϵ is going to change from material a to material b, the topological derivative of a functional J is defined as

$$D_T J^{a\to b}(\boldsymbol{z}) = \lim_{\epsilon\to 0} \frac{\delta J(\boldsymbol{z},\epsilon)}{g(\epsilon)}, \tag{20}$$

where $\delta J(\boldsymbol{z},\epsilon)$ is the perturbation of the value of J and $g(\epsilon)$ is a function of the radius ϵ, chosen so that the limit value of the right-hand side of Eq. (20) can exist. In this paper, we define $g(\epsilon)$ as the area of Ω_ϵ, as follows:

$$g(\epsilon) = \pi\epsilon^2. \tag{21}$$

Novotny et al. (2003) proposed a method for deriving the topological derivative from the relationship between the topological and shape derivatives. Following their method, we derive the topological derivative in the same way but for the optimum design problem given in Eqs. (15) and (18). The deduced topological derivatives can be expressed using the eigenvalues and eigenmodes, as follows:

$$D_T F^{a\to b} = -\left(\sum_{m=1}^{n} \frac{1}{\lambda_{(m)}}\right)^{-2} \sum_{m=1}^{n} \left(\frac{A_{ijkl}^{a\to b} \dfrac{\partial U_{(m)i}}{\partial x_j} \dfrac{\partial U_{(m)k}}{\partial x_l} + \lambda_{(m)}(\rho^a - \rho^b) U_{(m)i} U_{(m)i}}{\lambda_{(m)}^2} \right) \tag{22}$$

$$D_T G_k^{a\to b} = -\delta_{ka} + \delta_{kb} \tag{23}$$

$$D_T Gc^{a\to b} = A_{ijkl}^{a\to b} \frac{\partial u_i}{\partial x_j} \frac{\partial u_k}{\partial x_l}, \tag{24}$$

where the coefficients are derived as follows:

$$\begin{aligned} &A_{ijkl}^{a\to b} = A^{a\to b}\delta_{ij}\delta_{kl} + B^{a\to b}(\delta_{ik}\delta_{jl} + \delta_{il}\delta_{jk}) \\ &\begin{cases} A^{a\to b} = -\dfrac{E^{(a)}\left\{E^{(a)}(1-\nu^{(b)}) - E^{(b)}(1-\nu^{(a)})\right\}}{\left\{E^{(a)}(1-\nu^{(b)}) + E^{(b)}(1+\nu^{(a)})\right\}(1-\nu^{(a)})^2} + \dfrac{2E^{(a)}\left\{E^{(a)}(1+\nu^{(b)}) - E^{(b)}(1+\nu^{(a)})\right\}}{\left\{E^{(a)}(1+\nu^{(b)}) + E^{(b)}(3-\nu^{(a)})\right\}(1+\nu^{(a)})^2} \\ B^{a\to b} = -\dfrac{2E^{(a)}\left\{E^{(a)}(1+\nu^{(b)}) - E^{(b)}(1+\nu^{(a)})\right\}}{\left\{E^{(a)}(1+\nu^{(b)}) + E^{(b)}(3-\nu^{(a)})\right\}(1+\nu^{(a)})^2}. \end{cases} \end{aligned} \tag{25}$$

The topological derivative of the mean compliance in Eq. (24) has been already derived by Kishimoto et al. (2017), and the derivation of the topological derivative of the objective function Eq. (22) is followed by the numerical verification which can be found in Appendix A. Then, the topological derivative of the Lagrangian Eq. (19) can be expressed as

$$D_T \bar{F}^{a\to b} = D_T F^{a\to b} + \sum_{k=1}^{M} \left(\mu_k D_T G_k^{a\to b}\right) + \mu_{M+1} D_T Gc^{a\to b}. \tag{26}$$

[DOI: 10.1299/mej.22-00353]

3.2. Expression of the design sensitivity with topological derivatives

In this section, we recall the idea by Kishimoto et al (2017) and illustrate how the design sensitivity can be expressed based on topological derivatives. For brevity, we demonstrate the idea using a two-material case as an example. In this case, there are six topological derivatives that need to be computed: $D_T J^{1\to0}$, $D_T J^{2\to0}$, $D_T J^{0\to1}$, $D_T J^{0\to2}$, $D_T J^{1\to2}$, and $D_T J^{2\to1}$. The superscript "0" denotes a void region, and "1" and "2" denote solid phases #1 and #2, respectively (e.g.,$D_T J^{1\to0}$ is the topological derivative when an infinitesimal circular void region is created in solid phase #1, and so on).

As for $D_T J^{1\to0}$, $D_T J^{2\to0}$, $D_T J^{0\to1}$, $D_T J^{0\to2}$, the material distribution changes only from solid to void, or vice versa. But the material phase inside the solid region doesn't change. Therefore, for these topological changes, only the sign of the first level set function $\phi_1(\boldsymbol{x})$ changes, while that of the second level set function $\phi_2(\boldsymbol{x})$ does not. If we define $\delta\phi_1(\boldsymbol{x})$ as the perturbation of the first level set function $\phi_1(\boldsymbol{x})$, then $\mathrm{sign}\,(\delta\phi_1(\boldsymbol{x})) = -1$ for $D_T J^{1\to0}$ and $D_T J^{2\to0}$, and $\mathrm{sign}\,(\delta\phi_1(\boldsymbol{x})) = 1$ for $D_T J^{0\to1}$ and $D_T J^{0\to2}$. Therefore, the topological derivative with respect to $\phi_1(\boldsymbol{x})$ can be expressed as

$$\begin{aligned} J'^{(1)} &= \psi_1 \mathrm{sign}\,(\delta\phi_1(\boldsymbol{x}))\, D_T J^{1\to0} + \psi_2 \mathrm{sign}\,(\delta\phi_1(\boldsymbol{x}))\, D_T J^{2\to0} \\ &\quad + (1 - H(\phi_1))\left[(1 - H(\phi_2))\,\mathrm{sign}\,(\delta\phi_1(\boldsymbol{x}))\, D_T J^{0\to1} + H(\phi_2) D_T \mathrm{sign}\,(\delta\phi_1(\boldsymbol{x}))\, J^{0\to2}\right] \\ &= -\psi_1 D_T J^{1\to0} - \psi_2 D_T J^{2\to0} + (1 - H(\phi_1))\left[(1 - H(\phi_2))\, D_T J^{0\to1} + H(\phi_2) D_T J^{0\to2}\right]. \end{aligned} \tag{27}$$

As for $D_T J^{1\to2}$ and $D_T J^{2\to1}$, the material phase inside the solid region changes when there are no voids to be created. Therefore, only the sign of $\phi_2(\boldsymbol{x})$ can change, while that of $\phi_1(\boldsymbol{x})$ remains positive. Similarly, if we define $\delta\phi_2(\boldsymbol{x})$ as the perturbation of $\phi_2(\boldsymbol{x})$, then $\mathrm{sign}\,(\delta\phi_2(\boldsymbol{x})) = -1$ for $D_T J^{1\to2}$ and $\mathrm{sign}\,(\delta\phi_2(\boldsymbol{x})) = 1$ for $D_T J^{2\to1}$. Hence, the topological derivative with respect to $\phi_2(\boldsymbol{x})$ can be expressed as

$$\begin{aligned} J'^{(2)} &= \psi_2 \mathrm{sign}\,(\delta\phi_2(\boldsymbol{x}))\, D_T J^{2\to1} + H(\phi_1)(1 - H(\phi_2))\mathrm{sign}\,(\delta\phi_2(\boldsymbol{x}))\, D_T J^{1\to2} \\ &= -\psi_2 D_T J^{2\to1} + H(\phi_1)(1 - H(\phi_2)) D_T J^{1\to2}. \end{aligned} \tag{28}$$

In general, the topological derivative with respect to $\phi_i(\boldsymbol{x})$ for M phase materials can be expressed as

$$J'^{(i)} = -\sum_{j=i}^{M} \psi_j(\boldsymbol{x}) D_T J^{i\to(j-1)} + (1 - H(\phi_i(\boldsymbol{x})))\sum_{j=i}^{M} \frac{\partial \psi_j(\boldsymbol{x})}{\partial H(\phi_i(\boldsymbol{x}))} D_T J^{(j-1)\to i}. \tag{29}$$

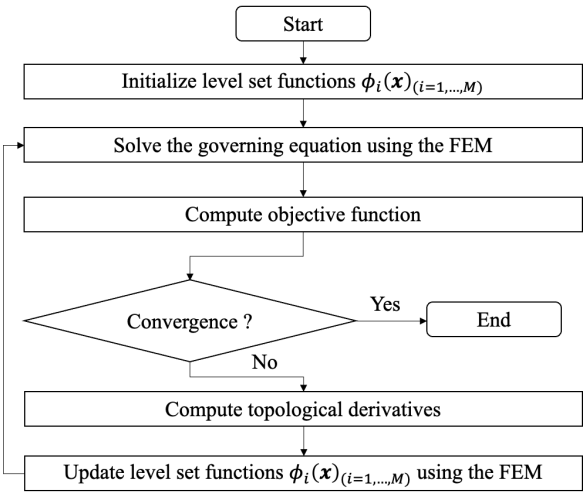

Fig. 5 Flowchart of topology optimization.

4. Numerical implementations

4.1. Optimization algorithms

The flowchart of the optimization procedure is shown in Fig. 5. First, the level set functions $\phi_i(\boldsymbol{x})$ are initialized. Then, the optimization loop begins. In the second step, the governing equations are solved using the finite element method. Next, the objective function is computed. The optimization loop is ended if the objective function has converged.

[DOI: 10.1299/mej.22-00353]

Otherwise, in the fourth step, the topological derivatives of the objective function and constraint functions are computed. Finally, the level set functions are updated based on Eq. (12) using the finite element method. This workflow will then be repeated until the stopping criteria is satisfied.

5. Numerical examples

5.1. Maximization of the fundamental eigenfrequency with concentrated masses

(a) Design model for the beam test case. (b) Initial guess. (c) Optimal structure.

Fig. 6 Topology optimization of a two-material beam structure.

In this section, we will show an example for the design problem illustrated in Section 2.5.1. We consider the optimization of a two-material beam structure to discuss the effects of different material properties on the optimal solutions. Secondly, a three-material beam design is presented.

In this paper, the Poisson's ratio of all the materials is set to 0.3, and the Young's modulus and mass density are non-dimentionalized. Both the Young's modulus and mass density of concentrated masses are set to 1.0×10^3. The eigenfrequency analysis is performed under plane stress conditions, and the objective function is the harmonic mean of the first three eigenvalues as defined in Eq. (14).

The target problem is a beam test case, as illustrated in Fig. 6a. The fixed design domain is a rectangular domain whose dimension is 6.0×1.0. Both the left and right ends are fixed walls, and a concentrated mass whose dimension is 0.05×0.05 is placed in the center of the design domain. Both the Young's modulus and mass density of material 1 (represented in blue color in the following figures) are set to 1.0 and those of material 2 (represented in red color in the following figures) are set to 2.0. The maximum allowed volume fractions for both materials 1 and 2 are set to $V^1_{max} = V^2_{max} = 0.2$, and the regularization parameters are set to $\tau_1 = \tau_2 = 1.0 \times 10^{-4}$.

Figs. 6b and c show the initial guess and the optimal structure, respectively, and Fig. 7 shows the first three eigenmodes of the optimal structure. The first and third eigenmodes are bending modes while the second one is a longitudinal mode. In the first eigenmodes, the large inertia force from the concentrated mass is applied to the structure in the direction perpendicular to the axis, resulting in the structure with a large moment of inertia of area near the concentrated mass and Γ_u, where the bending moment is large. We can observe that material 2, which has a higher stiffness, is placed near Γ_u, where the elastic strain energy density of the first eigenmode is relatively high. Material 1, which has a lower mass density, is placed away from Γ_u, where the amplitude of the first eigenmode is relatively large. Fig. 8a shows the convergence histories of the objective and constraint values, and Fig. 8b shows those of the first three eigenfrequencies. The value of the objective function of the optimal structure is $F = -7.710 \times 10^{-3}$, and the eigenfrequencies are $\omega_{(1)} = 1.017 \times 10^{-1}$, $\omega_{(2)} = 2.173 \times 10^{-1}$, and $\omega_{(3)} = 2.898 \times 10^{-1}$. From Fig. 8b, we can see that the eigenfrequencies do not change their order during this optimization process.

Here, we investigate the effect of the material properties on the optimal structure. Fig. 9 shows the optimal structures with different values of the mass density of material 2, while the material properties of material 1 and the Young's modulus of material 2 are the same as those cases shown in Fig. 6c. In each test case, the material with the lower mass density is distributed away from Γ_u, and the material with the higher mass density is distributed near Γ_u. However, the strain energy density is very high at the four corners of the design domain, therefore, the material with a higher stiffness is distributed there regardless of its mass density.

On the other hand, Fig. 10 shows the optimal structures with the different values of the Young's modulus of material

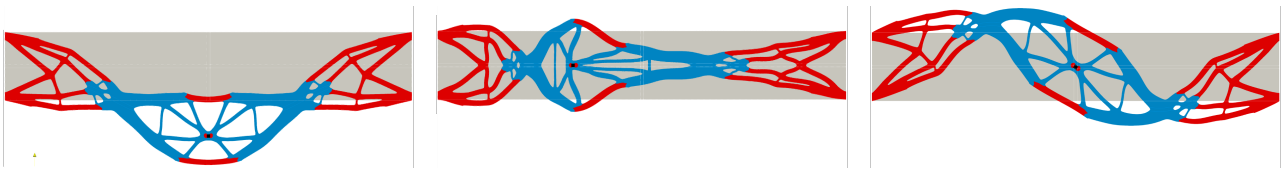

(a) 1st mode shape. (b) 2nd mode shape. (c) 3rd mode shape.

Fig. 7 Mode shapes of the optimal structure of a two-material beam problem.

[DOI: 10.1299/mej.22-00353]

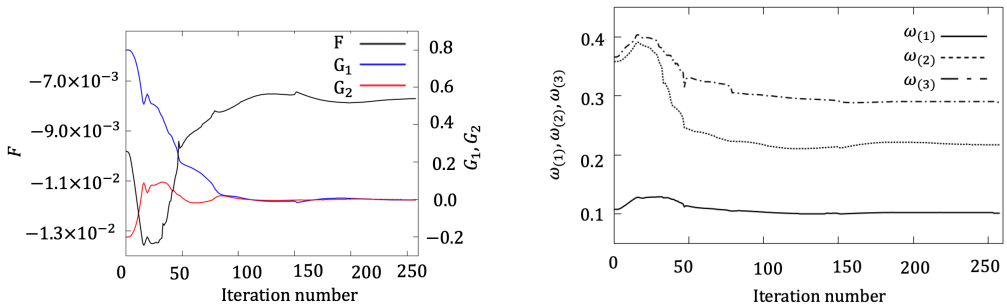

(a) Objective and constraint values. (b) First three eigenfrequencies.

Fig. 8 Histories of (a) the objective and constraint values, (b) the first three eigenfrequencies.

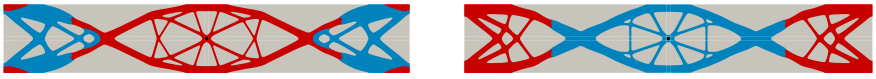

(a) $\rho_2 = 0.5$. (b) $\rho_2 = 8$.

Fig. 9 Optimal structures of material 2 with different values of mass density.

(a) $E_2 = 0.5$. (b) $E_2 = 4$.

Fig. 10 Optimal structures of material 2 with different values of Young's modulus.

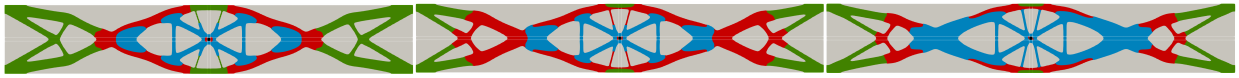

(a) $(V^1_{max}, V^2_{max}, V^3_{max}) = (0.1, 0.1, 0.2)$. (b) $(V^1_{max}, V^2_{max}, V^3_{max}) = (0.1, 0.2, 0.1)$. (c) $(V^1_{max}, V^2_{max}, V^3_{max}) = (0.2, 0.1, 0.1)$.

Fig. 11 Optimal structures of a three-material beam problem with different values of volume fractions.

2 while the other material properties remain unchanged. In both cases, the thicker structures composed of the softer material support the thinner structures composed of the stiffer material. As shown in Fig. 10b, materials with high mass density are distributed away from Γ_u if their Young's modulus is large, because these thin structures have an effect of its mass reduction. In actual design, the thin structures can collapse due to buckling or stress concentrations. One possible solution is to perform topology optimization with a buckling load constraint (Ferrari and Sigmund, 2019; Ishida et al., 2022) and a stress constraint (Le et al., 2010; Luo et al., 2013), but their applications are left for future work.

Finally, we examine the case where three materials are used. The Young's moduli of material 1 (blue regions), material 2 (red regions), and material 3 (green regions) are set to $E^{(1)} = 1$, $E^{(2)} = 2$, and $E^{(3)} = 3$, respectively, and the mass densities are $\rho^{(1)} = 1$, $\rho^{(2)} = 2$, and $\rho^{(3)} = 3$, respectively. The regularization parameters for all the level set functions are $\tau = 1 \times 10^{-4}$. Fig. 11 shows the optimal structure when the volume fractions are set to $\{V^1_{max}, V^2_{max}, V^3_{max}\} = \{0.1, 0.1, 0.2\}$, $\{0.1, 0.2, 0.1\}$, $\{0.2, 0.1, 0.1\}$. From these results, we can draw similar conclusions with the two-material cases. That is, the materials with higher stiffness are distributed near Γ_u, while the materials with lower mass density are distributed away from Γ_u. Therefore, it further confirms the validity of the proposed method.

5.2. Maximization of the fundamental eigenfrequency under mean compliance constraint

In this section, we will show an example for the design problem illustrated in Section 2.5.2. The effects of the direction of static traction force on the optimal solutions are examined.

Two target problems for maximization of the fundamental eigenfrequency under mean compliance constraint are shown in Fig. 12. Both the fixed design domains are a rectangular domain whose dimension is 2.0×1.0, the left end is fixed, $\boldsymbol{u} = [0, 0]^{\mathrm{T}}$, and traction $\bar{\boldsymbol{t}}$ is applied in the middle portion of the right end Γ_t. However, different traction $\bar{\boldsymbol{t}}$ is applied in model A and in model B: $\bar{\boldsymbol{t}} = [0, -1]^{\mathrm{T}}$ in model A and $\bar{\boldsymbol{t}} = [1, 0]^{\mathrm{T}}$ in model B. Both the Young's modulus and mass density of material 1 (represented in blue color in the following figures) are set to 1.0 and those of material 2 (represented in red color in the following figures) are set to 2.0. The maximum allowed volume fractions for both material phases are set to $V^1_{max} = V^2_{max} = 25\%$, and the regularization parameters are set to $\tau_1 = \tau_2 = 1.0 \times 10^{-4}$.

[DOI: 10.1299/mej.22-00353]

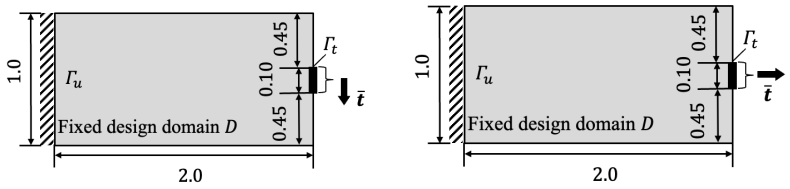

(a) Design model A. (b) Design model B.

Fig. 12 Design models for the cantilever test case.

Fig. 13a shows the initial guess for both models, and Figs. 13b and c show optimal structures of model A and model B, respectively. The objective value of the optimal structure of model A is $F = -8.103 \times 10^{-2}$ and that of model B is $F = -5.962 \times 10^{-2}$. Fig. 14 shows the first three eigenmodes of the optimal structure of model A, and the eigenfrequencies are $\omega_{(1)} = 3.343 \times 10^{-1}$, $\omega_{(2)} = 7.461 \times 10^{-1}$, and $\omega_{(3)} = 7.907 \times 10^{-1}$. On the other hand, Fig. 15 shows the first three eigenmodes of the optimal structure of model B, and the eigenfrequencies are $\omega_{(1)} = 2.802 \times 10^{-1}$, $\omega_{(2)} = 6.004 \times 10^{-1}$, and $\omega_{(3)} = 8.890 \times 10^{-1}$. Figs. 14 and 15 show that in the optimal solutions in both models, the first and second eigenmodes are bending modes while the third one is a longitudinal mode. The optimal solution of model A has a structure with a large moment of inertia of area, resulting in a structure with high stiffness against a bending load and bending vibration. Around Γ_t, where the amplitude of the first eigenmode is relatively large, material 1 is used because it has a lower mass density. On the other hand, in the optimal solution of model B, in order to increase stiffness against the axial load $\bar{t}$, the distribution of materials is concentrated around the axis of the cantilever and material 2 is placed near Γ_t, where strain energy density is relatively large. As a result, the optimal solution of model B has a smaller first eigenfrequency than the optimal solution of model A because the structure has less flexural rigidity and is heavier in the region away from Γ_u.

6. Conclusions

In this paper, we present a multi-material topology optimization (MMTO) method for the fundamental eigenfrequency maximization problem. The key idea is to adopt the RDE-based MMLS method to obtain the optimal configurations for multiple material phases represented by multiple level set functions. We formulated the MMTO problem in two different ways: (i) with concentrated mass and (ii) under mean compliance. We confirm the validity of the proposed

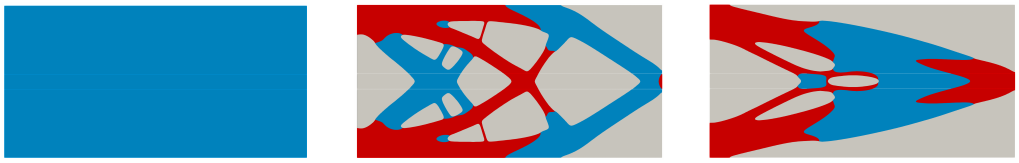

(a) Initial guess. (b) Optimal structure of model A. (c) Optimal structure of model B.

Fig. 13 Topology optimization of a two-material cantilever problem under mean compliance constraint.

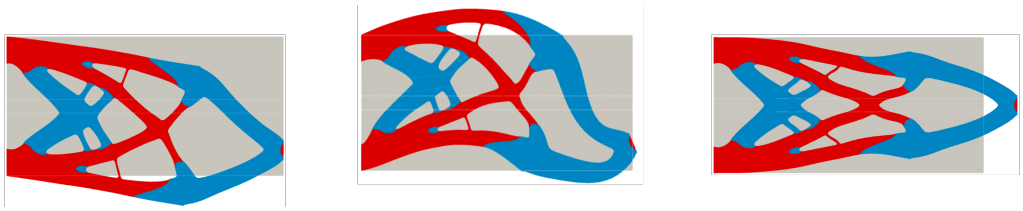

(a) 1st mode shape. (b) 2nd mode shape. (c) 3rd mode shape.

Fig. 14 Mode shapes of the optimal structure of model A.

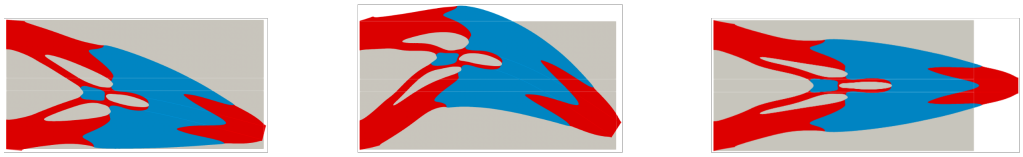

(a) 1st mode shape. (b) 2nd mode shape. (c) 3rd mode shape.

Fig. 15 Mode shapes of the optimal structure of model B.

[DOI: 10.1299/mej.22-00353]

methodology with concentrated masses by showcasing a beam example and the validity of the proposed methodology under mean compliance by a cantilever example. The main findings can be summarized as follows:

(1) MMLS method boundary representation allows us to obtain optimal configurations with clear boundaries between multiple material phases.

(2) Updating the level set function based on the reaction-diffusion equation in which the topological derivatives are used as the source term allows topological changes such that new holes can be created in the optimization process.

(3) It is confirmed that reasonable results can be obtained with different values of material properties and volume fractions. It is also shown that the proposed method can be easily extended to the case where not only two but also three materials are used.

(4) It is confirmed that imposing mean compliance constraints prevents the eigenfrequency problem in topology optimization from being an ill-posed problem. It is also found that different optimal structures are obtained for different static traction and that these structures are reasonable.

As a final remark, we conclude that many issues concerning eigenfrequency TO have still not been resolved and they are worthy of further investigation. For example, it could be quite interesting but challenging to extend the present framework to solve large-scale three-dimensional problems. This will require a fully distributed framework including scalable domain decomposition, matrix assembly, distributed unstructured mesh adaptation, etc. (Li et al., 2022c). And these are targeted in our future research works.

Acknowledgments

The authors gratefully acknowledge the financial support from the New Energy and Industrial Technology Development Organization (NEDO, JPNP14014).

References

Allaire, G., Jouve, F. and Toader, A.M., Structural optimization using sensitivity analysis and a level-set method, Journal of Computational Physics, Vol.194, No.1 (2004), pp.363-393.

Allaire, G., Jouve, F., A level-set method for vibration and multiple loads structural optimization, Computer Methods in Applied Mechanics and Engineering, Vol.194, No.30-33 (2005), pp.3269-3290.

Barber, J.R., Elasticity, Solid Mechanics and Its Applications, Vol.172 (2010).

Bendsøe, M.P. and Kikuchi, N., Generating optimal topologies in structural design using a homogenization method, Computer Methods in Applied Mechanics and Engineering, Vol.71, No.2 (1988), pp.197-224.

Bendsøe, M.P. and Sigmund, O., Material interpolation schemes in topology optimization, Archive of Applied Mechanics, Vol.69, No.9 (1999), pp.635-654.

Cui, M., Chen, H. and Zhou, J., A level-set based multi-material topology optimization method using a reaction diffusion equation, Computer Aided Design Vol.73 (2016), pp.41-52.

Díaaz, A. R., and Kikuchi, N., Solutions to shape and topology eigenvalue optimization problems using a homogenization method, International Journal for Numerical Methods in Engineering, Vol.35, No.7 (1992), pp.1487-1502.

Ferrari, F. and Sigmund, O., Revisiting topology optimization with buckling constraints. Structural and Multidisciplinary Optimization, Vol.59, No.5 (2019), pp.1401-1415.

Goede, M., Stehlin, M., Rafflenbeul, L., Kopp, G., and Beeh, E., Super Light Car—lightweight construction thanks to a multi-material design and function integration, European Transport Research Review, Vol.1, No.1 (2009), pp.5-10.

Giusti, S. M., Ferrer, A., and Oliver, J., Topological sensitivity analysis in heterogeneous anisotropic elasticity problem. Theoretical and computational aspects, Computer Methods in Applied Mechanics and Engineering, Vol.311 (2016), pp.134-150.

Guo, X., Zhang, W., and Zhong, W., Doing topology optimization explicitly and geometrically–a new moving morphable components based framework, Journal of Applied Mechanics, Vol.81(8) (2014), pp.081009.

Guo, X., Zhang, W., and Zhong, W., Stress-related topology optimization of continuum structures involving multi-phase materials, Computer Methods in Applied Mechanics and Engineering, Vol.268 (2014), pp.632-655.

Ishida, N., Kondoh, T., Furuta, K., Li, H., Izui, K., and Nishiwaki, S., Topology optimization for maximizing linear buckling load based on level set method. Mechanical Engineering Journal, Vol.9, No.4 (2022), pp.21-00425.

[DOI: 10.1299/mej.22-00353]

Kim, T. S., and Kim, Y. Y., Mac-based mode-tracking in structural topology optimization, Computers and Structures, Vol.74(3) (2000), pp.375-383.

Kishimoto, N., Noguchi, Y., Satou, Y., Izui, K., Yamada, T., Nishiwaki, S., Topology optimization for multi-material structures based on the level set method, Transactions of the Japan Society of Mechanical Engineers, Vol.83, No.849 (2017), pp.17-00069.

Le, C., Norato, J., Bruns, T., Ha, C., and Tortorelli, D., Stress-based topology optimization for continua. Structural and Multidisciplinary Optimization, Vol.41, No.4 (2010), pp.605-620.

Li, H., Yamada, T., Jolivet, P., Furuta, K., Kondoh, T., Izui, K., and Nishiwaki, S., Full-scale 3D structural topology optimization using adaptive mesh refinement based on the level-set method, Finite Elements in Analysis and Design, Vol.194, (2021), pp. 103561.

Li, H., Kondoh, T., Jolivet, P., Furuta K., Yamada, T., Zhu B., Zhang, H., Izui, K., and Nishiwaki, S., Optimum design and thermal modeling for 2D and 3D natural convection problems incorporating level set-based topology optimization with body-fitted mesh, International Journal for Numerical Methods in Engineering, Vol.123, No.9 (2022a), pp.1954–1990.

Li, H., Kondoh, T., Jolivet, P., Furuta, F., Yamada, T., Zhu, B., Izui, K., and Nishiwaki, S., Three-dimensional topology optimization of fluid–structure system using body-fitted mesh adaption based on the level-set method, Applied Mathematical Modelling, Vol.101, (2022b), pp.276–308.

Li, H., Kondoh, T., Jolivet, P., Nakayama, N., Furuta, K., Zhang, H., Zhu, B., Izui, K., and Nishiwaki, S., Topology optimization for lift–drag problems incorporated with distributed unstructured mesh adaptation, Structural and Multidisciplinary Optimization, Vol.65, No.8 (2022c), pp.222.

Luo, Z., Tong, L., Luo, J., Wei, P., and Wang, M. Y., Design of piezoelectric actuators using a multiphase level set method of piecewise constants, Journal of Computational Physics, Vol.228, No.7 (2009), pp.2643-2659.

Luo, Y., Wang, M. Y., and Kang, Z., An enhanced aggregation method for topology optimization with local stress constraints. Computer Methods in Applied Mechanics and Engineering, Vol.254 (2013), pp.31-41.

Ma, Z. D., Kikuchi, N., and Cheng, H. C., Topological Design for Vibrating Structures, Computer Methods in Applied Mechanics and Engineering, Vol.121 (1995), pp. 259–280.

Maeda, Y., Nishiwaki, S., Izui, K., Yoshimura, M., Matsui, K., and Terada, K., Structural topology optimization of vibrating structures with specified eigenfrequencies and eigenmode shapes, International Journal for Numerical Methods in Engineering, Vol.67, No.5 (2006), pp.597-628.

Novotny, A. A., Feijóo, R. A., Taroco, E., and Padra, C., Topological sensitivity analysis, Computer Methods in Applied Mechanics and Engineering, Vol.192, No.7-8 (2003), pp.803-829.

Pedersen, N. L., Maximization of eigenvalues using topology optimization, Structural and Multidisciplinary Optimization, Vol.20, No.1 (2000), pp.2-11.

Sigmund, O., and Torquato, S., Design of materials with extreme thermal expansion using a three-phase topology optimization method, Journal of the Mechanics and Physics of Solids, Vol.45, No.6 (1997), pp.1037-1067.

Wang, M.Y. and Wang, X., “Color” level sets: a multi-phase method for structural topology optimization with multiple materials, Computer Methods in Applied Mechanics and Engineering, Vol.193, No.6-8 (2004), pp.469-496.

Wang, M. Y., Chen, S., Wang, X., and Mei, Y., Design of multimaterial compliant mechanisms using level-set methods, Journal of Mechanical Design, Vol.127 (2005), pp.941–956

Wang, Y., Wang, X., and Guo, D., A level set method for structural topology optimization, Computer Methods in Applied Mechanics and Engineering, Vol.192 (2003), pp.227–246.

Wang, Y., Luo, Z, Kang, Z. and Zhang, N., A multi-material level set-based topology and shape optimization method, Computer Methods in Applied Mechanics and Engineering, Vol.283 (2015), pp.1570-1586.

Wei, P. and Wang, M.Y., Piecewise constant level set method for structural topology optimization, International Journal for Numerical Methods in Engineering, Vol.78, No.4 (2009), pp.379-402.

Xie, Y., and Steven, G.P., A simple evolutionary procedure for structural optimization, Computers and Structures, Vol.49(5) (1993), pp.885–896.

Xie, Y. M., and Steven, G. P., Evolutionary structural optimization for dynamic problems, Computers and Structures, Vol.58, No.6 (1996), pp.1067-1073.

Yamada, T., Izui, K., Nishiwaki, S., and Takezawa, A., A topology optimization method based on the level set method incorporating a fictitious interface energy, Computer Methods in Applied Mechanics and Engineering, Vol.199, No.45-48 (2010), pp.2876-2891.

[DOI: 10.1299/mej.22-00353]

Zhu, B., Wang, R., Wang, N., Li, H., Zhang, X., and Nishiwaki, S., Explicit structural topology optimization using moving wide Bezier components with constrained ends, Structural and Multidisciplinary Optimization, Vol.64 (2021), pp.53–70.

Appendix A Sensitivity analysis

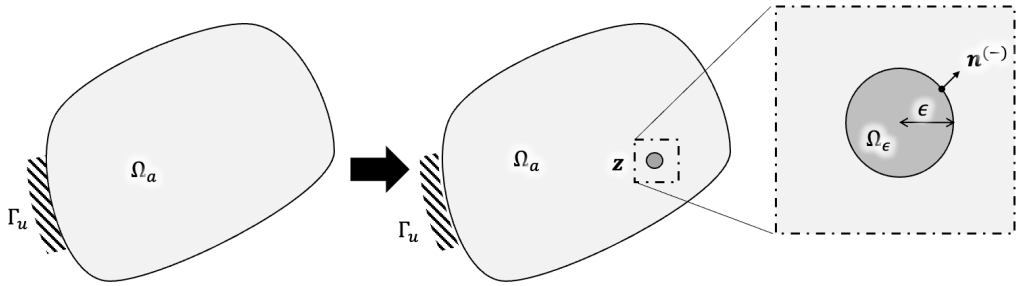

Fig. 16 Schematic diagram of topological derivative.

In the appendix, we provide the details of the sensitivity analysis. As stated in Section 3, the topological derivative at $\boldsymbol{z} \in \Omega_a$ is defined as follows:

$$D_T F^{a\to b}(\boldsymbol{z}) = \lim_{\epsilon\to 0} \frac{\delta F(\boldsymbol{z},\epsilon)}{g(\epsilon)}, \tag{A.1}$$

where $g(\epsilon)$ as the area of Ω_ϵ:

$$g(\epsilon) = \pi\epsilon^2. \tag{A.2}$$

In this section, we derive the topological derivative of F based on the method proposed by Novotny et al. (2003), on which the equation of the relationship between the topological derivative and shape derivative is used. The shape derivative is a functional derivative of an objective functional with respect to an infinitesimal change in its boundaries. The shape derivative is defined as follows:

$$DF(\Omega_a,\Omega_\epsilon)\cdot\boldsymbol{V} := \frac{d}{ds}F(\varphi_s(\Omega_a),\varphi_s(\Omega_\epsilon))\Big|_{s=0}, \tag{A.3}$$

where φ_s is deformation mapping of Ω_a and Ω_ϵ in the direction $\boldsymbol{V}(\boldsymbol{x})$, defined as:

$$\varphi_s(\boldsymbol{x}) = \boldsymbol{x} + s\boldsymbol{V}(\boldsymbol{x}). \tag{A.4}$$

In order to derive the topological derivative, we first calculate the shape derivative when Ω_ϵ expands isotropically. The vector $\boldsymbol{V}$ is then defined as follows:

$$\boldsymbol{V} = \boldsymbol{n}^{(-)} = -\boldsymbol{n}^{(+)} \text{ on } \Gamma_\epsilon, \tag{A.5}$$

where $\boldsymbol{n}^{(-)}$ is the outward unit normal vector at the boundary Γ_ϵ, as shown in Fig. 16. Novotny et al. (2003) proposed a method to derive the topological derivative by taking the limit value of the shape derivative when the radius ϵ approaches 0, as follows:

$$D_T F^{a\to b}(\boldsymbol{z}) = \lim_{\epsilon\to 0} \frac{DF(\Omega_a,\Omega_\epsilon)\cdot\boldsymbol{V}}{g'(\epsilon)}, \tag{A.6}$$

where $g'(\epsilon)$ is the derivative of $g(\epsilon)$ with respect to ϵ, which is $g'(\epsilon) = 2\pi\epsilon$ in this paper .

Assuming that the eigenfrequencies don't switch their orders due to the slight change in topology, the shape derivative of the objective function F in Eq. (14) is expressed as the sum of the shape derivatives of the eigenvalues:

$$DF(\Omega_a,\Omega_\epsilon)\cdot\boldsymbol{V} = \left(\sum_{m=1}^{n}\frac{1}{\lambda_{(m)}}\right)^{-2}\sum_{m=1}^{n}\left(\frac{D\lambda_{(m)}(\Omega_a,\Omega_\epsilon)\cdot\boldsymbol{V}}{\lambda_{(m)}^2}\right). \tag{A.7}$$

Therefore, the topological derivative of the objective function Eq. (14) is derived in the following process. First, we derive the shape derivative of the eigenvalue $\lambda_{(m)}$ using the adjoint variable method. Next, the asymptotic behavior of the state variables is examined as $\epsilon \to 0$. Finally, we substitute the result of the asymptotic analysis into the shape derivative, and obtain the topological derivative from the relationship between the shape derivative and topological derivative of Eq. (A.6).

[DOI: 10.1299/mej.22-00353]

A.1 Formulation of Lagrangian

We consider eigenvalues and eigenvectors after the material in Ω_ϵ changes from material a to material b. If we represent the eigenvalues and eigenvectors by adding superscript ϵ to them, the governing equations underlying the mth eigenvalue $\lambda^\epsilon_{(m)}$ and the corresponding eigenmode $\boldsymbol{U}^\epsilon_{(m)}$ can be formulated as the following boundary value problem:

$$C^{(b)}_{ijkl}\frac{\partial^2 U^\epsilon_{(m)k}}{\partial x_l \partial x_j} + \lambda^\epsilon_{(m)}\rho^{(b)}U^\epsilon_{(m)i} = 0 \text{ in } \Omega_\epsilon \tag{A.8a}$$

$$C^{(a)}_{ijkl}\frac{\partial^2 U^\epsilon_{(m)k}}{\partial x_l \partial x_j} + \lambda^\epsilon_{(m)}\rho^{(a)}U^\epsilon_{(m)i} = 0 \text{ in } \Omega_a \backslash \Omega_\epsilon \tag{A.8b}$$

$$U^{\epsilon(-)}_{(m)i} - U^{\epsilon(+)}_{(m)i} = 0 \text{ on } \Gamma_\epsilon \tag{A.8c}$$

$$C^{(b)}_{ijkl}\frac{\partial U^{\epsilon(-)}_{(m)k}}{\partial x_l}n^{(\epsilon)}_j - C^{(a)}_{ijkl}\frac{\partial U^{\epsilon(+)}_{(m)k}}{\partial x_l}n^{(\epsilon)}_j = 0 \text{ on } \Gamma_\epsilon \tag{A.8d}$$

$$U^\epsilon_{(m)i} = 0 \text{ on } \Gamma_u \tag{A.8e}$$

$$C_{ijkl}\frac{\partial U_{(m)k}}{\partial x_l}n_j = 0 \text{ on } \Gamma_n, \tag{A.8f}$$

where the quantities with superscript $(-)$ represent quantities inside Ω_ϵ, and the quantities with superscript $(+)$ represent quantities outside Ω_ϵ. The eigenmodes are normalized as follows:

$$\int_{\Omega_a}(\rho^{(a)}U^\epsilon_{(m)i}U^\epsilon_{(m)i})d\Omega + \int_{\Omega_\epsilon}(\rho^{(b)}U^\epsilon_{(m)i}U^\epsilon_{(m)i})d\Omega = 1 \tag{A.9}$$

In order to derive the shape derivative of the eigenvalue $\lambda^\epsilon_{(m)}$, we formulate the Lagrangian L as

$$\begin{aligned} L\left(\Omega_a, \Omega_\epsilon; \boldsymbol{W}, X, \tilde{\boldsymbol{W}}, \tilde{X}\right) = \quad & X + \int_{\Omega_a}\left(C^{(a)}_{ijkl}\frac{\partial \tilde{W}_i}{\partial x_j}\frac{\partial W_k}{\partial x_l} - X\rho^{(a)}\tilde{W}_i W_i\right)d\Omega + \int_{\Omega_\epsilon}\left(C^{(b)}_{ijkl}\frac{\partial \tilde{W}_i}{\partial x_j}\frac{\partial W_k}{\partial x_l} - X\rho^{(b)}\tilde{W}_i W_i\right)d\Omega \\ & - \int_{\Gamma_\epsilon}\frac{1}{2}\left(C^{(a)}_{ijkl}\frac{\partial W^{(+)}_k}{\partial x_l}n^{(+)}_j - C^{(b)}_{ijkl}\frac{\partial W^{(-)}_k}{\partial x_l}n^{(-)}_j\right)\left(\tilde{W}^{(+)}_i - \tilde{W}^{(-)}_i\right)d\Gamma \\ & - \int_{\Gamma_\epsilon}\frac{1}{2}\left(C^{(a)}_{ijkl}\frac{\partial \tilde{W}^{(+)}_i}{\partial x_j}n^{(+)}_l - C^{(b)}_{ijkl}\frac{\partial \tilde{W}^{(-)}_i}{\partial x_j}n^{(-)}_l\right)\left(W^{(+)}_k - W^{(-)}_k\right)d\Gamma \\ & - \int_{\Gamma_u}\left(C^{(a)}_{ijkl}\frac{\partial W_k}{\partial x_l}n_j\right)\tilde{W}_i d\Gamma - \int_{\Gamma_u}\left(C^{(a)}_{ijkl}\frac{\partial \tilde{W}_i}{\partial x_j}n_l\right)W_k d\Gamma \\ & + \tilde{X}\left\{1 - \int_{\Omega_a}(\rho^{(a)}W_i W_i)d\Omega - \int_{\Omega_\epsilon}(\rho^{(b)}W_i W_i)d\Omega\right\}. \end{aligned} \tag{A.10}$$

Note that $\boldsymbol{W}, X, \tilde{\boldsymbol{W}}, \tilde{X}$ are variables independent of Ω_a and Ω_ϵ, whereas $\boldsymbol{U}_{(m)}$ and $\lambda_{(m)}$ are the state variables that depend on Ω_a and Ω_ϵ.

Performing integration by parts with respect to $\tilde{\boldsymbol{W}}$, the Lagrangian (A.10) can be transformed as

$$\begin{aligned} L\left(\Omega_a, \Omega_\epsilon; \boldsymbol{W}, X, \tilde{\boldsymbol{W}}, \tilde{X}\right) = \quad & X - \int_{\Omega_a}\left(C^{(a)}_{ijkl}\frac{\partial^2 W_k}{\partial x_l \partial x_j} + X\rho^{(a)}W_i\right)\tilde{W}_i d\Omega - \int_{\Omega_\epsilon}\left(C^{(b)}_{ijkl}\frac{\partial^2 W_k}{\partial x_l \partial x_j} + X\rho^{(b)}W_i\right)\tilde{W}_i d\Omega \\ & + \int_{\Gamma_\epsilon}\frac{1}{2}\left(C^{(a)}_{ijkl}\frac{\partial W^{(+)}_k}{\partial x_l}n^{(+)}_j + C^{(b)}_{ijkl}\frac{\partial W^{(-)}_k}{\partial x_l}n^{(-)}_j\right)\left(\tilde{W}^{(+)}_i - \tilde{W}^{(-)}_i\right)d\Gamma \\ & - \int_{\Gamma_\epsilon}\frac{1}{2}\left(C^{(a)}_{ijkl}\frac{\partial \tilde{W}^{(+)}_i}{\partial x_j}n^{(+)}_l - C^{(b)}_{ijkl}\frac{\partial \tilde{W}^{(-)}_i}{\partial x_j}n^{(-)}_l\right)\left(W^{(+)}_k - W^{(-)}_k\right)d\Gamma \\ & + \int_{\Gamma_n}\left(C^{(a)}_{ijkl}\frac{\partial W_k}{\partial x_l}n_j\right)\tilde{W}_i d\Gamma - \int_{\Gamma_u}\left(C^{(a)}_{ijkl}\frac{\partial \tilde{W}_i}{\partial x_j}n_l\right)W_k d\Gamma \\ & + \tilde{X}\left\{1 - \int_{\Omega_a}(\rho^{(a)}W_i W_i)d\Omega - \int_{\Omega_\epsilon}(\rho^{(b)}W_i W_i)d\Omega\right\}. \end{aligned} \tag{A.11}$$

From the governing equations Eqs. (A.8a) to (A.8f) and the normalization condition Eq. (A.9), we can see that the following equation is varied for any $\tilde{\boldsymbol{W}}$ and $\tilde{X}$ if $\boldsymbol{W} = \boldsymbol{U}^\epsilon_{(m)}(\Omega_a, \Omega_\epsilon)$ and $X = \lambda^\epsilon_{(m)}(\Omega_a, \Omega_\epsilon)$:

$$\lambda^\epsilon_{(m)}(\Omega_a, \Omega_\epsilon) = L\left(\Omega_a, \Omega_\epsilon; \boldsymbol{u}^\epsilon_{(m)}, \lambda^\epsilon_{(m)}, \boldsymbol{W}, \tilde{X}\right). \tag{A.12}$$

[DOI: 10.1299/mej.22-00353]

A.2 Adjoint variable

At the stationary point of the Lagrangian, the following stationary conditions are valid:

$$\left\langle \frac{\partial L}{\partial W_i}, \delta W_i \right\rangle = 0, \tag{A.13}$$

$$\frac{\partial L}{\partial X} = 0, \tag{A.14}$$

$$\left\langle \frac{\partial L}{\partial \tilde{W}_i}, \delta \tilde{W}_i \right\rangle = 0, \tag{A.15}$$

$$\frac{\partial L}{\partial \tilde{X}} = 0. \tag{A.16}$$

From Eq. (A.11) and stationary conditions Eqs. (A.15) and (A.16), the following equations can be obtained:

$$\begin{aligned}
0 &= \left\langle \frac{\partial L}{\partial W_i}, \delta W_i \right\rangle \\
&= \int_{\Omega_a} \left(C^{(a)}_{ijkl} \frac{\partial^2 W_k}{\partial x_l \partial x_j} + X \rho^{(a)} W_i \right) \delta \tilde{W}_i d\Omega + \int_{\Omega_\epsilon} \left(C^{(b)}_{ijkl} \frac{\partial^2 W_k}{\partial x_l \partial x_j} + X \rho^{(b)} W_i \right) \delta \tilde{W}_i d\Omega \\
&- \int_{\Gamma_\epsilon} \frac{1}{2} \left(C^{(a)}_{ijkl} \frac{\partial W^{(+)}_k}{\partial x_l} n^{(+)}_j + C^{(b)}_{ijkl} \frac{\partial W^{(-)}_k}{\partial x_l} n^{(-)}_j \right) (\delta \tilde{W}^{(+)}_i - \delta \tilde{W}^{(-)}_i) d\Gamma \\
&- \int_{\Gamma_\epsilon} \frac{1}{2} (W^{(+)}_k - W^{(-)}_k) \left(C^{(a)}_{ijkl} \frac{\partial \left(\delta \tilde{W}^{(+)}_i \right)}{\partial x_j} n^{(+)}_l - C^{(b)}_{ijkl} \frac{\partial \left(\delta \tilde{W}^{(-)}_i \right)}{\partial x_j} n^{(-)}_l \right) d\Gamma \\
&+ \int_{\Gamma_n} \left(C^{(a)}_{ijkl} \frac{\partial W_k}{\partial x_l} n_j \right) \delta \tilde{W}_i d\Gamma - \int_{\Gamma_u} W_k \left(C^{(a)}_{ijkl} \frac{\partial \left(\delta \tilde{W}_i \right)}{\partial x_j} n_l \right) d\Gamma,
\end{aligned} \tag{A.17}$$

$$0 = \frac{\partial L}{\partial \tilde{X}} = 1 - \int_{\Omega_a} (\rho^{(a)} W_i W_i) d\Omega - \int_{\Omega_\epsilon} (\rho^{(b)} W_i W_i) d\Omega. \tag{A.18}$$

Comparing the above equations with the governing equations Eqs. (A.8a) to (A.8f) and the normalization condition Eq. (A.9), we can see that $\boldsymbol{W} = \boldsymbol{U}^{\epsilon}_{(m)}(\Omega_a, \Omega_\epsilon)$ and $X = \lambda^{\epsilon}_{(m)}(\Omega_a, \Omega_\epsilon)$ satisfy the stationary conditions Eqs. (A.15) and (A.16) for any $\delta\tilde{\boldsymbol{W}}$ and δX.

Next, we consider the stationary conditions Eqs. (A.13) and (A.14). We assume that the stationary conditions are valid if $\tilde{\boldsymbol{W}} = \boldsymbol{v}(\Omega_a, \Omega_\epsilon)$ and $\tilde{X} = \eta(\Omega_a, \Omega_\epsilon)$. Using integration by parts, the Lagrangian Eq. (A.10) can be deformed as follows:

$$\begin{aligned}
L(\Omega_a, \Omega_\epsilon; \boldsymbol{W}, X, \tilde{\boldsymbol{W}}, \tilde{X}) = \quad & X - \int_{\Omega_a} \left(C^{(a)}_{ijkl} \frac{\partial^2 \tilde{W}_i}{\partial x_j \partial x_l} + X \rho^{(a)} \tilde{W}_k \right) W_k d\Omega - \int_{\Omega_a} \left(C^{(a)}_{ijkl} \frac{\partial^2 \tilde{W}_i}{\partial x_j \partial x_l} + X \rho^{(a)} \tilde{W}_k \right) W_k d\Omega \\
& - \int_{\Gamma_\epsilon} \frac{1}{2} \left(C^{(a)}_{ijkl} \frac{\partial W^{(+)}_k}{\partial x_l} n^{(+)}_j - C^{(b)}_{ijkl} \frac{\partial W^{(-)}_k}{\partial x_l} n^{(-)}_j \right) (\tilde{W}^{(+)}_i - \tilde{W}^{(-)}_i) d\Gamma \\
& + \int_{\Gamma_\epsilon} \frac{1}{2} \left(C^{(a)}_{ijkl} \frac{\partial \tilde{W}^{(+)}_i}{\partial x_j} n^{(+)}_l + C^{(b)}_{ijkl} \frac{\partial \tilde{W}^{(-)}_i}{\partial x_j} n^{(-)}_l \right) (W^{(+)}_k - W^{(-)}_k) d\Gamma \\
& + \int_{\Gamma_n} \left(C^{(a)}_{ijkl} \frac{\partial \tilde{W}_i}{\partial x_j} n_l \right) W_k d\Gamma - \int_{\Gamma_u} \left(C^{(a)}_{ijkl} \frac{\partial W_k}{\partial x_l} n_j \right) \tilde{W}_i d\Gamma \\
& + \tilde{X} \left\{ 1 - \int_{\Omega_a} (\rho^{(a)} W_i W_i) d\Omega - \int_{\Omega_\epsilon} (\rho^{(b)} W_i W_i) d\Omega \right\}.
\end{aligned} \tag{A.19}$$

From the above equation and the stationary conditions Eqs. (A.13) and (A.14), the following equality is obtained:

[DOI: 10.1299/mej.22-00353]

$$
\begin{aligned}
0 &= \left\langle \frac{\partial L}{\partial W_i}, \delta W_i \right\rangle \\
&= \int_{\Omega_a} \left(C^{(a)}_{ijkl} \frac{\partial^2 v_k}{\partial x_l \partial x_j} + \lambda^{\epsilon}_{(m)} \rho^{(a)} v_i + 2\eta \rho^{(a)} U^{\epsilon}_{(m)i} \right) \delta W_i d\Omega + \int_{\Omega_\epsilon} \left(C^{(b)}_{ijkl} \frac{\partial^2 v_k}{\partial x_l \partial x_j} + \lambda^{\epsilon}_{(m)} \rho^{(b)} v_i + 2\eta \rho^{(b)} U^{\epsilon}_{(m)i} \right) \delta W_i d\Omega \\
&- \int_{\Gamma_\epsilon} \frac{1}{2} (v_k^{(+)} - v_k^{(-)}) \left(C^{(a)}_{ijkl} \frac{\partial \left(\delta W_i^{(+)} \right)}{\partial x_j} n_l^{(+)} - C^{(b)}_{ijkl} \frac{\partial \left(\delta W_i^{(-)} \right)}{\partial x_j} n_l^{(-)} \right) d\Gamma \\
&+ \int_{\Gamma_\epsilon} \frac{1}{2} \left(C^{(a)}_{ijkl} \frac{\partial v_k^{(+)}}{\partial x_l} n_j^{(+)} + C^{(b)}_{ijkl} \frac{\partial v_k^{(-)}}{\partial x_l} n_j^{(-)} \right) (\delta W_i^{(+)} - \delta W_i^{(-)}) d\Gamma \\
&+ \int_{\Gamma_n} \left(C^{(a)}_{ijkl} \frac{\partial v_k}{\partial x_l} n_j \right) \delta W_i d\Gamma - \int_{\Gamma_u} v_k \left(C^{(a)}_{ijkl} \frac{\partial (\delta W_i)}{\partial x_j} n_l \right) d\Gamma,
\end{aligned}
\tag{A.20}
$$

$$
0 = \frac{\partial L}{\partial X} = 1 - \int_{\Omega_a} \left(\rho^{(a)} v_i U^{\epsilon}_{(m)i} \right) d\Omega - \int_{\Omega_\epsilon} \left(\rho^{(b)} v_i U^{\epsilon}_{(m)i} \right) d\Omega. \tag{A.21}
$$

Here, we used the fact that $C_{ijkl} = C_{klij}$ to convert the subscript (i, j, k, l) to (k, l, i, j). Therefore, the stationary conditions Eqs. (A.13) and (A.14) are valid when $\boldsymbol{v}$ and η satisfy the following adjoint equation:

$$
C^{(b)}_{ijkl} \frac{\partial^2 v_k}{\partial x_l \partial x_j} + \lambda \rho^{(b)} v_i + 2\eta \rho^{(a)} U^{\epsilon}_{(m)i} = 0 \text{ in } \Omega_\epsilon \tag{A.22a}
$$

$$
C^{(a)}_{ijkl} \frac{\partial^2 v_k}{\partial x_l \partial x_j} + \lambda \rho^{(a)} v_i + 2\eta \rho^{(a)} U^{\epsilon}_{(m)i} = 0 \text{ in } \Omega_a \backslash \Omega_\epsilon \tag{A.22b}
$$

$$
v^{(+)}_{(m)i} - v^{(-)}_{(m)i} = 0 \text{ on } \Gamma_\epsilon \tag{A.22c}
$$

$$
C^{(+)}_{ijkl} \frac{\partial v_k^{(a)}}{\partial x_l} n_j^{(+)} + C^{(b)}_{ijkl} \frac{\partial v_k^{(-)}}{\partial x_l} n_j^{(-)} = 0 \text{ on } \Gamma_\epsilon \tag{A.22d}
$$

$$
v_i = 0 \text{ on } \Gamma_u \tag{A.22e}
$$

$$
C_{ijkl} \frac{\partial v_k}{\partial x_l} n_j = 0 \text{ on } \Gamma_n \tag{A.22f}
$$

$$
\int_{\Omega_a} (\rho^{(a)} v_i U^{\epsilon}_{(m)i}) d\Omega + \int_{\Omega_\epsilon} (\rho^{(b)} v_i U^{\epsilon}_{(m)i}) d\Omega = 1, \tag{A.22g}
$$

Now, we determine the value of η. The following equation can be obtained by multiplying Eqs. (A.8a) and (A.8b) by $\boldsymbol{v}$ and integrating it over the domain:

$$
\int_{\Omega_a} \left(C^{(a)}_{ijkl} \frac{\partial v_i}{\partial x_j} \frac{\partial U^{\epsilon}_{(m)k}}{\partial x_l} - \lambda \rho^{(a)} v_i U^{\epsilon}_{(m)i} \right) d\Omega + \int_{\Omega_\epsilon} \left(C^{(b)}_{ijkl} \frac{\partial v_i}{\partial x_j} \frac{\partial U^{\epsilon}_{(m)k}}{\partial x_l} - \lambda \rho^{(b)} v_i U^{\epsilon}_{(m)i} \right) d\Omega = 0. \tag{A.23}
$$

The following equality is obtained by multiplying the adjoint equations Eqs. (A.22a) and (A.22b) by $\boldsymbol{u}^{\epsilon}_{(m)}$ and integrating it:

$$
\int_{\Omega_a} \left(C^{(a)}_{ijkl} \frac{\partial v_i}{\partial x_j} \frac{\partial U^{\epsilon}_{(m)k}}{\partial x_l} - \lambda \rho^{(a)} U^{\epsilon}_{(m)i} v_i - 2\eta U^{\epsilon}_{(m)i} U^{\epsilon}_{(m)i} \right) d\Omega + \int_{\Omega_\epsilon} \left(C^{(b)}_{ijkl} \frac{\partial v_i}{\partial x_j} \frac{\partial U^{\epsilon}_{(m)k}}{\partial x_l} - \lambda \rho^{(b)} U^{\epsilon}_{(m)i} v_i - 2\eta U^{\epsilon}_{(m)i} U^{\epsilon}_{(m)i} \right) d\Omega = 0 \tag{A.24}
$$

By taking the difference between Eq. (A.23) and Eq. (A.24) and using the normalization condition Eq. (A.9), η can be obtained as

$$
\eta \left\{ \int_{\Omega_a} (\rho^{(a)} U^{\epsilon}_{(m)i} U^{\epsilon}_{(m)i}) d\Omega + \int_{\Omega_\epsilon} (\rho^{(b)} U^{\epsilon}_{(m)i} U^{\epsilon}_{(m)i}) d\Omega \right\} = \eta = 0. \tag{A.25}
$$

Hence, the adjoint equations Eqs. (A.22a) to (A.22g) are equal to the governing equations Eqs. (A.8a) to (A.8f) and the normalization condition Eq. (A.9). Therefore, the adjoint variable can be expressed with the eigenmode multiplied with a constant K, as follows:

$$
\boldsymbol{v} = K \boldsymbol{U}^{\epsilon}_{(m)}. \tag{A.26}
$$

[DOI: 10.1299/mej.22-00353]

Furthermore, from the normalization conditions for the eigenmode and the adjoint variable Eqs. (A.9) and (A.22g), the value of K can be determined as follows:

$$\begin{aligned} 1 &= \int_{\Omega_a} \left(\rho^{(a)} U^{\epsilon}_{(m)i} v_i\right) d\Omega + \int_{\Omega_\epsilon} \left(\rho^{(b)} U^{\epsilon}_{(m)i} v_i\right) d\Omega \\ &= K \left\{ \int_{\Omega_a} \left(\rho^{(a)} U^{\epsilon}_{(m)i} U^{\epsilon}_{(m)i}\right) d\Omega + \int_{\Omega_\epsilon} \left(\rho^{(b)} U^{\epsilon}_{(m)i} U^{\epsilon}_{(m)i}\right) d\Omega \right\} \\ &= K. \end{aligned} \tag{A.27}$$

Therefore, the adjoint variable is equal to the eigenmode:

$$\boldsymbol{v} = \boldsymbol{U}^{\epsilon}_{(m)}. \tag{A.28}$$

A.3 Shape derivative

We derive the shape derivative of the eigenvalue $\lambda_{(m)}$ from the shape derivative of the Lagrangian at the stationary point. We use the following formulas for shape derivatives (Allaire et al., 2004). If the functional J is defined as the domain integral over the domain Ω of a density function $j(\boldsymbol{x})$, as follows:

$$J = \int_\Omega j d\Omega, \tag{A.29}$$

then the shape derivative of J can be obtained as

$$DJ \cdot \boldsymbol{V} = \int_{\partial\Omega} (V_i n_i) j d\Omega, \tag{A.30}$$

where $\boldsymbol{n}$ denotes the outward unit normal vector on $\partial\Omega$. On the other hand, if the functional J is defined as the boundary integral of a density function $j(\boldsymbol{x})$, as follows:

$$J = \int_\Gamma j d\Gamma, \tag{A.31}$$

then the shape derivative of J is obtained as

$$DJ \cdot \boldsymbol{V} = \int_{\partial\Omega} (V_i n_i) \left(\frac{\partial j}{\partial x_j} n_j + H j \right) d\Omega, \tag{A.32}$$

where $H \equiv \mathrm{div}\boldsymbol{n}$ is the mean curvature of $\partial\Omega$. The formulas Eqs. (A.30) and (A.32) can be used only if the density function $j(\boldsymbol{x})$ does not depend on Ω.

From Eq. (A.12), the shape derivative of the eigenvalue $\lambda_{(m)}$ can be derived from the shape derivative of the Lagrangian at the stationary point, as follows:

$$\begin{aligned} D\lambda^{\epsilon}_{(m)}(\Omega_a, \Omega_\epsilon) \cdot \boldsymbol{V} &= DL(\Omega_a, \Omega_\epsilon) \cdot \boldsymbol{V} |_{\boldsymbol{W}=\boldsymbol{U}^{\epsilon}_{(m)}, X=\lambda^{\epsilon}_{(m)}, \tilde{\boldsymbol{W}}=\boldsymbol{U}^{\epsilon}_{(m)}, \tilde{X}=0} \\ &\quad + \left\langle \frac{\partial L}{\partial W_i}(\Omega_a, \Omega_\epsilon), \delta W_i \right\rangle \Big|_{\boldsymbol{W}=\boldsymbol{U}^{\epsilon}_{(m)}, X=\lambda^{\epsilon}_{(m)}, \tilde{\boldsymbol{W}}=\boldsymbol{U}^{\epsilon}_{(m)}, \tilde{X}=0} + \frac{\partial L}{\partial X}(\Omega_a, \Omega_\epsilon) \cdot \delta X \Big|_{\boldsymbol{W}=\boldsymbol{U}^{\epsilon}_{(m)}, X=\lambda^{\epsilon}_{(m)}, \tilde{\boldsymbol{W}}=\boldsymbol{U}^{\epsilon}_{(m)}, \tilde{X}=0} \\ &\quad + \left\langle \frac{\partial L}{\partial \tilde{W}_i}(\Omega_a, \Omega_\epsilon), \delta \tilde{W}_i \right\rangle \Big|_{\boldsymbol{W}=\boldsymbol{U}^{\epsilon}_{(m)}, X=\lambda^{\epsilon}_{(m)}, \tilde{\boldsymbol{W}}=\boldsymbol{U}^{\epsilon}_{(m)}, \tilde{X}=0} + \frac{\partial L}{\partial \tilde{X}}(\Omega_a, \Omega_\epsilon) \cdot \delta \tilde{X} \Big|_{\boldsymbol{W}=\boldsymbol{U}^{\epsilon}_{(m)}, X=\lambda^{\epsilon}_{(m)}, \tilde{\boldsymbol{W}}=\boldsymbol{U}^{\epsilon}_{(m)}, \tilde{X}=0} \\ &= DL(\Omega_a, \Omega_\epsilon) \cdot \boldsymbol{V} |_{\boldsymbol{W}=\boldsymbol{U}^{\epsilon}_{(m)}, X=\lambda^{\epsilon}_{(m)}, \tilde{\boldsymbol{W}}=\boldsymbol{U}^{\epsilon}_{(m)}, \tilde{X}=0}, \end{aligned} \tag{A.33}$$

Here, we used the fact that the second to fifth terms of the middle side of the above equation are zero for any $\delta\boldsymbol{W}, \delta X, \delta\tilde{\boldsymbol{W}}, \delta\tilde{X}$ from the stationary conditions Eqs. (A.13) to (A.16). Applying the shape derivative formulas Eq. (A.30) and Eq. (A.32) to the shape derivative of the Lagrangian, and noting that $\boldsymbol{U}^{\epsilon(+)}_{(m)} = \boldsymbol{U}^{\epsilon(-)}_{(m)}$ and $C^{(a)}_{ijkl} \dfrac{\partial U^{\epsilon(+)}_{(m)k}}{\partial x_l} n^{(+)}_j = -C^{(b)}_{ijkl} \dfrac{\partial U^{\epsilon(-)}_{(m)k}}{\partial x_l} n^{(-)}_j$ on the boundary Γ_ϵ and the vector field $\boldsymbol{V}$ is defined as Eq. (A.5), the shape derivative of the eigenvalue $\lambda^{\epsilon}_{(m)}$ can be expressed as

$$\begin{aligned} D\lambda^{\epsilon}_{(m)}(\Omega_a, \Omega_\epsilon) \cdot \boldsymbol{V} = &\int_{\Gamma_\epsilon} \left(C^{(b)}_{ijkl} \frac{\partial U^{\epsilon(-)}_{(m)i}}{\partial x_j} \frac{\partial U^{\epsilon(-)}_{(m)k}}{\partial x_l} - \lambda^{\epsilon}_{(m)} \rho^{(b)} U^{\epsilon(-)}_{(m)i} U^{\epsilon(-)}_{(m)i} \right) d\Gamma \\ &- \int_{\Gamma_\epsilon} \left(C^{(a)}_{ijkl} \frac{\partial U^{\epsilon(+)}_{(m)i}}{\partial x_j} \frac{\partial U^{\epsilon(+)}_{(m)k}}{\partial x_l} - \lambda^{\epsilon}_{(m)} \rho^{(a)} U^{\epsilon(+)}_{(m)i} U^{\epsilon(+)}_{(m)i} \right) d\Gamma \\ &- \int_{\Gamma_\epsilon} 2 \left(C^{(b)}_{ijkl} \frac{\partial U^{(-)}_{(m)k}}{\partial x_l} n^{(-)}_j \right) \left(\frac{\partial U^{(-)}_{(m)i}}{\partial x_\beta} n^{(-)}_\beta - \frac{\partial U^{(+)}_{(m)i}}{\partial x_\beta} n^{(-)}_\beta \right) d\Gamma. \end{aligned} \tag{A.34}$$

[DOI: 10.1299/mej.22-00353]

A.4 Asymptotic analysis

In this step, the asymptotic behavior of the state variables $\boldsymbol{U}^{\epsilon}_{(m)}$ and $\lambda^{\epsilon}_{(m)}$ is examined when the radius ϵ approaches 0. $\boldsymbol{U}^{\epsilon}_{(m)}$ and $\lambda^{\epsilon}_{(m)}$ are expanded using the eigenmode and eigenvalue when Ω_ϵ does not exist, as follows:

$$\begin{aligned} \boldsymbol{U}^{\epsilon}_{(m)}(\boldsymbol{x}) &= \boldsymbol{U}_{(m)}(\boldsymbol{x}) + \hat{\boldsymbol{U}}(\boldsymbol{x}), \\ \lambda^{\epsilon}_{(m)} &= \lambda_{(m)} + \hat{\lambda}, \end{aligned} \tag{A.35}$$

where $\boldsymbol{U}_{(m)}$ and $\lambda_{(m)}$ are the mth eigenmode and eigenvalue, respectively, when Ω_ϵ does not exist, whereas $\hat{\boldsymbol{U}}$ and $\hat{\lambda}$ are remainders. Now, we introduce a new coordinate $\boldsymbol{\xi} = \dfrac{\boldsymbol{x}-\boldsymbol{z}}{\epsilon}$, and $\hat{\boldsymbol{U}}$ can be expanded asymptotically with respect to ϵ (Giusti et al., 2016):

$$\hat{\boldsymbol{U}}(\boldsymbol{x}) = \hat{\boldsymbol{w}}(\boldsymbol{\xi}) = \epsilon\hat{\boldsymbol{w}}^{(0)}(\boldsymbol{\xi}) + O(\epsilon^2), \tag{A.36}$$

Moreover, $\boldsymbol{U}_{(m)}$ can be Taylor-expanded in a neighborhood of $\boldsymbol{z}$, as follows:

$$U_{(m)i}(\boldsymbol{x}) = U_{(m)i}(\boldsymbol{z}) + \epsilon\xi_j \left.\frac{\partial U_{(m)i}}{\partial x_j}\right|_{\boldsymbol{x}=\boldsymbol{z}} + \epsilon^2\xi_j\xi_k \left.\frac{\partial^2 U_{(m)i}}{\partial x_j \partial x_k}\right|_{\boldsymbol{x}=\boldsymbol{z}} + O(\epsilon^3). \tag{A.37}$$

By substituting Eqs. (A.36) and (A.37) into Eqs. (A.8a) and (A.8b), the following equations for $\hat{\boldsymbol{w}}(\boldsymbol{\xi})$ are obtained:

$$C^{(b)}_{ijkl}\left.\frac{\partial^2 U_{(m)k}}{\partial x_l \partial x_j}\right|_{\boldsymbol{x}=\boldsymbol{z}} + \frac{C^{(b)}_{ijkl}}{\epsilon^2}\frac{\partial^2 \hat{w}^{(-)}_k(\boldsymbol{\xi})}{\partial\xi_l\partial\xi_j} + \left(\lambda_{(m)}+\hat{\lambda}\right)\rho^{(b)}\left\{U_{(m)i}(\boldsymbol{z}) + \hat{w}^{(-)}_i(\boldsymbol{\xi})\right\} + O(\epsilon) = 0 \text{ in } \Omega_\epsilon, \tag{A.38a}$$

$$\frac{C^{(a)}_{ijkl}}{\epsilon^2}\frac{\partial^2 \hat{w}^{(+)}_k(\boldsymbol{\xi})}{\partial\xi_l\partial\xi_j} + \lambda_{(m)}\rho^{(p)}\hat{w}^{(+)}_i(\boldsymbol{\xi}) + \hat{\lambda}\rho^{(a)}\left\{U_{(m)i}(\boldsymbol{z}) + \hat{w}^{(+)}_i(\boldsymbol{\xi})\right\} + O(\epsilon) = 0 \text{ in } \Omega_a\backslash\Omega_\epsilon. \tag{A.38b}$$

The leading term, $\hat{\boldsymbol{w}}^{(0)}$, satisfies the following equations:

$$C^{(b)}_{ijkl}\frac{\partial^2 \hat{w}^{(0)(-)}_k(\boldsymbol{\xi})}{\partial\xi_l\partial\xi_j} = 0 \text{ in } \Omega_\epsilon \tag{A.39a}$$

$$C^{(a)}_{ijkl}\frac{\partial^2 \hat{w}^{(0)(+)}_k(\boldsymbol{\xi})}{\partial\xi_l\partial\xi_j} = 0 \text{ in } \Omega_a\backslash\Omega_\epsilon. \tag{A.39b}$$

From Eqs. (A.39a) and (A.39b), we can see that the partial differential equation for the leading term $\hat{\boldsymbol{w}}^{(0)}$ is the same as that of static equilibrium problems. Similarly, the boundary condition for $\hat{\boldsymbol{w}}^{(0)}$ on Γ_ϵ can be obtained as

$$\hat{w}^{(0)(-)}_i(\boldsymbol{\xi}) - \hat{w}^{(0)(+)}_i(\boldsymbol{\xi}) = 0 \text{ on } \Gamma_\epsilon \tag{A.40a}$$

$$C^{(b)}_{ijkl}\left\{\left.\frac{\partial U_{(m)k}}{\partial x_l}\right|_{\boldsymbol{x}=\boldsymbol{z}} n^{(-)}_j + \frac{\partial \hat{w}^{(-)}_k(\boldsymbol{\xi})}{\partial\xi_l}n^{(-)}_j\right\} - C^{(a)}_{ijkl}\left\{\left.\frac{\partial U_{(m)k}}{\partial x_l}\right|_{\boldsymbol{x}=\boldsymbol{z}} n^{(-)}_j + \frac{\partial \hat{w}^{(+)}_k(\boldsymbol{\xi})}{\partial\xi_l}n^{(-)}_j\right\} = 0 \text{ on } \Gamma_\epsilon. \tag{A.40b}$$

To obtain the explicit expression for $\hat{\boldsymbol{w}}^{(0)}$, it is required that $\hat{w}^{(0)(+)}_i \to 0$ when $r = \sqrt{\xi_1^2+\xi_2^2} \to \infty$. The boundary value problem for $\hat{\boldsymbol{w}}^{(0)}$ can be solved in polar coordinates (r,θ) defined as follows:

$$\xi_1 = r\cos(\theta),\ \xi_2 = r\sin(\theta) \tag{A.41}$$

Using the analytical solution of static equilibrium problems for the linear elastic model in the polar coordinate system (Barber, 2010), $\hat{\boldsymbol{w}}^{(0)}$ can be calculated as

$$\begin{aligned} \hat{w}^{(0)(-)}_r &= D_1 r + D_2\kappa^{(a)} r\cos(2\theta) + D_3\kappa^{(a)} r\sin(2\theta), \\ \hat{w}^{(0)(-)}_\theta &= -D_2\kappa^{(a)} r\sin(2\theta) + D_3\kappa^{(a)} r\cos(2\theta), \\ \hat{w}^{(0)(+)}_r &= D_1 r^{-1} + D_2\left\{(\kappa^{(a)}+1)r^{-1} - r^{-3}\right\}\cos(2\theta) + D_3\left\{(\kappa^{(a)}+1)r^{-1} - r^{-3}\right\}\sin(2\theta), \\ \hat{w}^{(0)(+)}_\theta &= -D_2\left\{(\kappa^{(a)}-1)r^{-1} + r^{-3}\right\}\sin(2\theta) + D_3\left\{(\kappa^{(a)}-1)r^{-1} + r^{-3}\right\}\cos(2\theta), \end{aligned} \tag{A.42}$$

where the coefficients are

$$\begin{aligned} D_1 &= \frac{E^{(a)}(1-\nu^{(b)}) - E^{(b)}(1-\nu^{(a)})}{E^{(a)}(1-\nu^{(b)}) + E^{(b)}(1+\nu^{(a)})}\left(\left.\frac{\partial U_{(m)1}}{\partial x_1}\right|_{\boldsymbol{x}=\boldsymbol{z}} + \left.\frac{\partial U_{(m)2}}{\partial x_2}\right|_{\boldsymbol{x}=\boldsymbol{z}}\right), \\ D_2 &= \frac{E^{(a)}(1+\nu^{(b)}) - E^{(b)}(1+\nu^{(a)})}{2\left\{E^{(a)}(1+\nu^{(b)}) + E^{(b)}(3-\nu^{(a)})\right\}}\left(\left.\frac{\partial U_{(m)1}}{\partial x_1}\right|_{\boldsymbol{x}=\boldsymbol{z}} - \left.\frac{\partial U_{(m)2}}{\partial x_2}\right|_{\boldsymbol{x}=\boldsymbol{z}}\right), \\ D_3 &= \frac{E^{(a)}(1+\nu^{(b)}) - E^{(b)}(1+\nu^{(a)})}{2\left\{E^{(a)}(1+\nu^{(b)}) + E^{(b)}(3-\nu^{(a)})\right\}}\left(\left.\frac{\partial U_{(m)1}}{\partial x_2}\right|_{\boldsymbol{x}=\boldsymbol{z}} + \left.\frac{\partial U_{(m)2}}{\partial x_1}\right|_{\boldsymbol{x}=\boldsymbol{z}}\right). \end{aligned} \tag{A.43}$$

[DOI: 10.1299/mej.22-00353]

A.5 Topological derivative

The asymptotic behavior of the shape derivative Eq. (A.34) can be calculated using the results of the asymptotic analysis of the eigenmode $\boldsymbol{U}^{\epsilon}_{(m)}$, as follows:

$$D\lambda^{\epsilon}_{(m)}(\Omega_a, \Omega_\epsilon)\cdot \boldsymbol{V} = 2\pi\epsilon\left\{A^{a\to b}_{ijkl}\frac{\partial U_{(m)i}}{\partial x_j}\frac{\partial U_{(m)k}}{\partial x_l} + \lambda_{(m)}(\rho^a-\rho^b)U_{(m)i}U_{(m)i}\right\} + O(\epsilon^2), \tag{A.44}$$

where the coefficients are

$$\begin{aligned} &A^{a\to b}_{ijkl} = A^{a\to b}\delta_{ij}\delta_{kl} + B^{a\to b}(\delta_{ik}\delta_{jl}+\delta_{il}\delta_{jk}) \\ &\begin{cases} A^{a\to b} = \dfrac{E^{(a)}\left\{E^{(a)}(1-\nu^{(b)}) - E^{(b)}(1-\nu^{(a)})\right\}}{\{E^{(a)}(1-\nu^{(b)}) + E^{(b)}(1+\nu^{(a)})\}(1-\nu^{(a)})^2} + \dfrac{2E^{(a)}\left\{E^{(a)}(1+\nu^{(b)}) - E^{(b)}(1+\nu^{(a)})\right\}}{\{E^{(a)}(1+\nu^{(b)}) + E^{(b)}(3-\nu^{(a)})\}(1+\nu^{(a)})^2} \\ B^{a\to b} = \dfrac{2E^{(a)}\left\{E^{(a)}(1+\nu^{(b)}) - E^{(b)}(1+\nu^{(a)})\right\}}{\{E^{(a)}(1+\nu^{(b)}) + E^{(b)}(3-\nu^{(a)})\}(1+\nu^{(a)})^2}. \end{cases} \end{aligned} \tag{A.45}$$

From the relation in Eq. (A.7), the shape derivative of the objective function F is obtained using the shape derivative of the eigenvalues as

$$DF(\Omega_a, \Omega_\epsilon)\cdot \boldsymbol{V} = -2\pi\epsilon\left(\sum_{m=1}^{n}\frac{1}{\lambda_{(m)}}\right)^{-2}\sum_{m=1}^{n}\left(\frac{A^{a\to b}_{ijkl}\dfrac{\partial U_{(m)i}}{\partial x_j}\dfrac{\partial U_{(m)k}}{\partial x_l} + \lambda_{(m)}(\rho^a-\rho^b)U_{(m)i}U_{(m)i}}{\lambda^2_{(m)}}\right) + O(\epsilon^2). \tag{A.46}$$

Based on the relationship between the topological derivative and the shape derivative in Eq. (A.6), the topological derivative can be obtained by taking the limit value of the shape derivative, as follows:

$$D_T F = -\left(\sum_{m=1}^{n}\frac{1}{\lambda_{(m)}}\right)^{-2}\sum_{m=1}^{n}\left(\frac{A^{a\to b}_{ijkl}\dfrac{\partial U_{(m)i}}{\partial x_j}\dfrac{\partial U_{(m)k}}{\partial x_l} + \lambda_{(m)}(\rho^a-\rho^b)U_{(m)i}U_{(m)i}}{\lambda^2_{(m)}}\right). \tag{A.47}$$

Appendix B Numerical validation of topological derivatives

Here, we numerically validate the topological derivative of F in Eq. (A.47), by comparing the results obtained using the derivatives with those obtained using finite differences. Consider that Ω_r is a circular region with a finite radius r whose center is located at $\boldsymbol{z}$, as shown in Fig. 17. The numerical finite difference is the sensitivity of the objective function when Ω_r is replaced with a different material. Therefore, the numerical finite difference can be defined as

$$D_N F^{a\to b}(\boldsymbol{z}, r) = \frac{\delta F(z, r)}{g(r)}. \tag{B.48}$$

In Fig. 18, the black points indicate the values of the topological derivative and the red points indicate the values of the numerical difference. We can see that the numerical difference and topological derivative take the same values, therefore, the validity of the topological derivative we derived is confirmed.

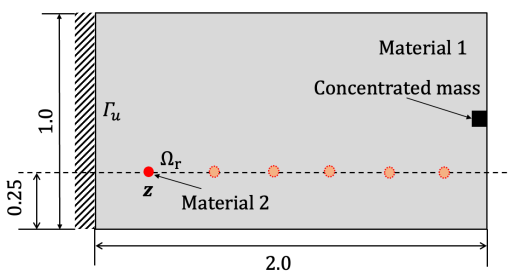

Fig. 17 Schematic diagram of numerical difference.

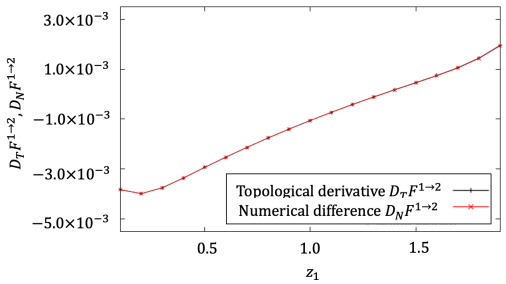

Fig. 18 Comparison between topological derivative and numerical difference.

[DOI: 10.1299/mej.22-00353]